J. Fluid Mech. (2013), *vol.* 733, *pp.* 325–369.
doi:10.1017/jfm.2013.428

Toward second-moment closure modelling of compressible shear flows

Carlos A. Gomez and Sharath S. Girimaji†

Department of Aerospace Engineering, Texas A&M University, College Station, TX 77843-3141, USA

(Received 24 April 2012; revised 1 August 2013; accepted 12 August 2013;
first published online 23 September 2013)

Compressibility profoundly affects many aspects of turbulence in high-speed flows, most notably stability characteristics, anisotropy, kinetic–potential energy interchange and spectral cascade rate. We develop a unified framework for modelling pressure-related compressibility effects by characterizing the role and action of pressure in different speed regimes. Rapid distortion theory is used to examine the physical connection between the various compressibility effects leading to model form suggestions for pressure–strain correlation, pressure–dilatation and dissipation evolution equations. The closure coefficients are established using fixed-point analysis by requiring consistency between model and DNS asymptotic behaviour in compressible homogeneous shear flow. The closure models are employed to compute high-speed mixing layers and boundary layers. The self-similar mixing-layer profile, increased Reynolds stress anisotropy and diminished mixing-layer growth rates with increasing Mach number are all well captured. High-speed boundary-layer results are also adequately replicated even without the use of advanced thermal-flux models or low-Reynolds-number corrections.

Key words: compressible turbulence, shear layer turbulence, turbulence modelling

1. Introduction

In high-speed flows the complex phenomenon of turbulence is further exacerbated by compressibility effects engendered by the changing nature of pressure in different speed regimes. At low speeds, the role of pressure is to simply uphold the divergence-free state of the velocity field. Consequently, in low-Mach-number flows pressure is merely a Lagrange multiplier governed by the Poisson equation. As we progress to higher flow speeds, the nature of pressure changes drastically. Pressure becomes a *bona fide* thermodynamic variable that is governed collectively by the energy equation, equation of state and calorific equation of state (see figure 1). At these high speeds, pressure assumes wave-like characteristics leading to intricate interactions with the velocity field resulting in a profound modification to the nature of turbulence.

The objective of the current work is to develop practical high-fidelity closure models for high-speed compressible shear flows. Much of our current understanding of turbulence flow physics and resulting closure model development is in the context of incompressible velocity and Poisson pressure fields. Attempts at modelling compressibility effects as straightforward extensions of incompressible models have

† Email address for correspondence: girimaji@tamu.edu

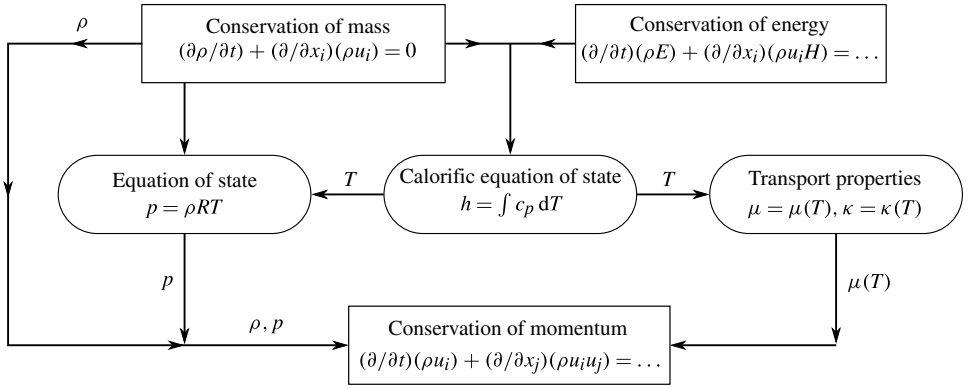

FIGURE 1. Dynamics of compressible flows.

only been marginally successful. The lack of closure modelling success can be attributed to the inability to account for the change in the pressure paradigm at higher speeds. Compressible flow closure modelling must necessarily involve three distinct steps: (i) identification of the critical compressibility physics absent at lower speeds; (ii) development of a unified closure framework in which various compressibility features can be incorporated into the model in a self-consistent manner; and (iii) establishment of the cause–effect relationship between closure coefficients and resulting model behaviour leading to a clear validation road map.

In categorizing the different types of turbulence models, we adopt the terminology given in the review papers of Reynolds (1976) and Speziale (1991). Speziale points out that all Reynolds-averaged Navier–Stokes (RANS)-based closure models are phenomenological in nature but the degree of empiricism varies with the level of closure. Typically, zero, one, and two-equation models invoke a constitutive relation (e.g. Boussinessq approximation) that completely omits history and non-local effects. Further, such closures do not explicitly account for the action of pressure which is critical in the presence of extra effects such as streamline curvature, frame rotation and compressibility. Accordingly, zero, one and two-equation models are considered empirical closures (in decreasing order of severity). At the level of second-moment closure (SMC), an evolution equation is used to determine the turbulent stresses. Integration over the evolution trajectories intrinsically incorporates history and non-locality (advection) effects into the stresses. Explicit models for rapid and slow pressure–strain correlation effects add further fidelity. Although SMC modelling of pressure effects does involve a certain degree of empiricism, physical fidelity can be enhanced by requiring consistency with mathematical principles such as realizability (Lumley 1978; Girimaji 2004) and physical theories such as rapid distortion theory (RDT). Using RDT as the guiding principle for rapid pressure–strain correlation modelling has led to important progress in incorporating the physics of frame rotation, streamline curvature and other body forces into SMC calculations of turbulent flows. In the terminology of Speziale (1991), it is therefore reasonable to refer to such SMC modelling as more physics-based. Our goal in this work is to follow this proven physics-based paradigm to incorporate compressibility effects into SMC closures by requiring close similitude to compressible RDT results.

1.1. *Relevant compressible physics*

High-speed and compressibility effects profoundly alter archetypal turbulence, which is the subject of a multitude of studies in literature. Most importantly, the flow develops a dilatational component of velocity field that can lead to shocks, density variations and other effects. Variations in transport coefficients as a function of temperature can also be significant for compressible flows. For a given equation of state, any distinction between incompressible and compressible turbulence must be manifested only through pressure and transport coefficients. In recent years, many of the consequences of compressibility on turbulence have been examined in high-speed shear flows using rapid distortion theory and direct numerical simulation (Cambon, Coleman & Mansour 1993; Sarkar 1995; Livescu, Jaberi & Madnia 2002; Pantano & Sarkar 2002; Lavin *et al.* 2012; Lee & Girimaji 2013; Bertsch, Suman & Girimaji 2012).

Comprehensive modelling of compressible turbulence must address: (i) pressure effects; (ii) transport coefficient effects; and (iii) near-wall phenomena. Each of the three categories represents a distinctly different physical process and can be modelled independently. Pressure effects are expected to be dominant in free shear flows and the other two can be significant in wall-bounded flows. In this work we focus on pressure-related effects.

We now identify four important pressure-related aspects of compressible turbulence that are most relevant for engineering applications and hence must be among the first to be incorporated into practical closure models. (i) The flow field is coupled with thermodynamic variables leading to strong interactions between conservation of mass, momentum and energy equations. The flow–thermodynamics interactions lead to interchange between kinetic and potential (pressure field) energies. (ii) Compressible turbulence exhibits a much higher degree of velocity fluctuation anisotropy than incompressible turbulence under similar conditions. The degree of anisotropy increases with Mach number. (iii) It is now well established that compressible shear flows are more stable than their incompressible counterparts. (iv) The classical Kolmogorov energy cascade picture may not be valid in compressible turbulence due to the above kinetic–potential energy exchanges. It is vital that all these interconnected phenomena be incorporated into closure models in a self-consistent manner.

Compressibility effects pertaining to the energy equation, transport coefficients, and near-wall effects are not considered in this study. The constituent phenomena of these effects are distinct from pressure effects and their model development can proceed independently.

1.2. *Second-moment closure framework*

Second-moment closure (Reynolds 1976) represents the lowest turbulence description level at which various compressible unclosed phenomena such as pressure–strain correlation and pressure–dilatation can be isolated and modelled with some degree of fidelity to the underlying physics. Despite the recent advances in direct numerical simulations (DNS) and large-eddy simulations (LES), Reynolds-averaged Navier–Stokes methods such as SMC continue to be used extensively for practical applications. Lower-order RANS models can be systematically derived from SMC using the weak equilibrium assumption (Pope 1975; Rodi 1976; Gatski & Speziale 1993; Girimaji 1996, 1997; Gatski & Jongen 2000; Wallin & Johansson 2000) rendering any advances in SMC invaluable to the entire hierarchy of RANS methods. In recent times, variable-resolution (VR) approaches that optimally combine the advantages of LES and RANS are gaining prominence for engineering computations.

The use of VR methods is expected to increase and this approach may indeed emerge as the most viable computational design tool of the future. Many VR closures (Chaouat & Schiestel 2005; Girimaji 2006; Girimaji, Jeong & Srinivasan 2006) can be derived formally from a parent RANS closure employing the averaging invariance principle (Germano 1992; Suman & Girimaji 2010). Any improvements in SMC models can be incorporated to VR methods. Furthermore, SMC can also serve as the basis of Langevin and probability density function (p.d.f.) methods (Durbin & Speziale 1994; Pope 1994). Thus, SMC developments continue to be important for both near-term RANS and long-term VR turbulence computations. In the SMC approach, flow stabilization and anisotropization are manifested through the pressure–strain correlation (Sarkar 1995; Pantano & Sarkar 2002); flow–thermodynamics interaction and kinetic–potential energy exchange is brought about by pressure–dilatation; and the change in the spectral cascade rate affects the dissipation rate equation. Therefore, we restrict our focus in this study to the closure modelling of pressure–strain correlation, pressure–dilatation, and dissipation.

Pressure–strain correlation modelling is commonly considered the biggest challenge to accurately computing complex turbulent flows. Although much progress has been made for incompressible flows (Launder, Reece & Rodi 1975; Speziale, Sarkar & Gatski 1991; Johansson & Hallbäck 1994; Ristorcelli, Lumley & Abid 1995; Girimaji 2000; Sjögren & Johansson 2000), finding an adequate compressible pressure–strain correlation has proven to be an elusive task. Some of the earliest work towards the development of a compressible pressure–strain correlation closure is that done by Cambon *et al.* (1993) and Adumitroaie, Ristorcelli & Taulbee (1999). Cambon *et al.* (1993) propose an exponential decay of the rapid pressure–strain correlation as a function of gradient Mach number. Their model is found to agree well with DNS of axially compressed turbulence. Adumitroaie *et al.* (1999) incorporate the effects of pressure–dilatation, compressible dissipation, and mass flux in Favre-averaged SMC simulations of two-dimensional high-speed mixing layers. Their work considers modelling of various SMC unclosed terms in the weakly compressible limit of turbulence. In this treatment, pressure is represented by an expansion about the Poisson-equation-dictated incompressible base state. Closure models for pressure-related terms at this limiting state of compressible turbulence were derived using perturbation analysis. Away from the weak compressibility limit, these closure models are not valid and a more comprehensive approach is needed for higher Mach numbers. For example, this model does not address the wave nature of pressure that is critically important at higher Mach number. Although Adumitroaie *et al.* (1999) are able to obtain good agreement with mixing-layer growth rates, their compressibility corrections decrease the streamwise Reynolds stress of high-speed shear layers, contrary to the results observed in experiments (Goebel & Dutton 1991) and DNS (Freund, Lele & Moin 2000; Pantano & Sarkar 2002).

In a series of studies, Sarkar and co-workers (Sarkar, Erlebacher & Hussaini 1991*a*; Sarkar 1995; Pantano & Sarkar 2002) demonstrate that many of the compressibility effects in shear turbulence are due to changes in the character of the pressure–strain correlation. Pantano & Sarkar (2002) propose that for mixing layers the ratio of compressible to incompressible pressure–strain correlation components depends on the relative Mach number: $M_r \equiv \Delta U/\overline{a} = 2(U_1 - U_2)/[(a_1 + a_2)]$, where the subscripts 1 and 2 denote the high- and low-speed inlets respectively, U is the mean velocity, and a is the speed of sound. Other researchers have attempted to address compressibility effects by modifying incompressible models with a blending function based on turbulent Mach number (Fujiwara, Matsuo & Chuichi 2000; Marzougui, Khlifi & Lili 2005;

Park & Park 2005; Huang & Fu 2008; Kim & Park 2010; Khlifi *et al.* 2011), $M_t \equiv \sqrt{2k}/a$, where k is the turbulent kinetic energy. All authors report reduced spreading rates for compressible mixing layers and overall better agreement with experimental data when compared to standard incompressible models.

Examples of dissipation (or equivalently length scale) equation modelling in compressible flows include the early work of Sarkar *et al.* (1991*a*) and more recently Aupoix (2004). While these models have yielded some plausible results such as reduction in mixing-layer thickness, concomitant effects pertaining to increase in anisotropy or the exchange of energy between kinetic and potential (thermodynamic) forms are not explained. It is now widely recognized that the dominant compressibility effect is manifested via the pressure–strain correlation (Sarkar 1995).

1.3. *Present work*

The main features of this work are now introduced.

Closure modelling framework. In this work we present a unified framework for the development of physics-based closure models for the various manifestations of compressibility effects: pressure–strain correlation (stabilization and anisotropy), pressure–dilatation (kinetic–potential energy transfer) and corrections to the dissipation equation (spectral cascade modification). The framework is based on the recognition of the changing behaviour of pressure in different Mach-number regimes and identification of the consequent effects on turbulence. Specifically, the interaction/coupling between pressure and inertial physics is examined as pressure goes from a thermodynamic variable in high-speed flows to a Lagrange multiplier whose only role is to impose the dilatation-free constraint on the velocity field at low speeds. The framework proposal draws heavily on many DNS results (Simone, Coleman & Cambon 1997; Freund *et al.* 2000; Pantano & Sarkar 2002; Lee & Girimaji 2013) and RDT analyses (Bertsch 2010; Lavin *et al.* 2012; Bertsch *et al.* 2012) to characterize the behaviour of pressure in various speed regimes. At very high Mach numbers, pressure effects are insignificant in comparison with inertial effects. At very low Mach numbers, it can be argued that pressure acts rapidly to prevent any change in the divergence of the velocity field. At intermediate Mach numbers, pressure evolves according to a wave equation. In this regime, flow–thermodynamics interactions can be complex and the pressure–strain correlation needs to be modelled appropriately. Thus, a physics-based SMC model must necessarily account for the changing character of the pressure–strain correlation, pressure–dilatation and consequent changes in the spectral cascade rate at the various regimes. Practical considerations require that we start from a standard incompressible pressure–strain correlation closure form and add dilatational terms suggested by RDT and DNS findings. Once the pressure–strain correlation model is established, the pressure–dilatation model is obtained by taking the trace. The modification to the dissipation equation comes from the consideration of what constitutes a spectral cascade in compressible turbulence. The model proposal is based on the argument that any kinetic energy converted to internal energy by the action of pressure–dilatation will not contribute to the cascade. Thus, the models of the various compressibility effects are derived in a self-consistent manner using a unified closure framework.

Fixed-point analysis. An important step in the development process is to establish the closure model coefficients for the broadest range of applicability. Compressible homogeneous shear flow is a quintessential member of the shear flow family that contains the gist of the dominant physics resident in other members (Sarkar 1995). Fixed-point analysis (Girimaji 2000) can be used to establish the causal relationship

between model coefficients and the asymptotic model behaviour in homogeneous flows. While such analysis has been widely used in incompressible flows (Speziale 1991; Speziale *et al.* 1991; Speziale, Gatski & Sarkar 1992; Girimaji 2000), it has not been extended to compressible flows. In this study, we extend fixed-point analysis to compressible shear turbulence. This causal relationship is employed to determine the model coefficients as functions of gradient Mach number. The coefficients are determined by seeking consistency between the model fixed-point behaviour and the self-similar DNS asymptotic-state anisotropy in compressible homogeneous shear flow.

Closure model validation. The model is used to compute transient homogeneous shear flow behaviour and high-speed mixing and boundary layers. The model results are validated against DNS and experimental data in the above three flows. Remarkably, the pressure–strain correlation coefficients require no modification from the compressible homogeneous shear DNS calibrations to accurately capture the supersonic mixing-layer spreading rates and therefore the Langley curve (Kline, Cantwell & Lilley 1982). Its performance in high-speed boundary layers is also quite adequate even without accounting for near-wall effects.

The outline of the paper is as follows. Section 2 presents the SMC equations for compressible turbulence and identifies the terms that require closure modelling. The underlying physics of each closure term is discussed in § 3. In § 4, the closure models are developed and the coefficients are determined by comparing model fixed points with long time behaviour of compressible homogeneous shear DNS. Validation of the model in supersonic compressible mixing and boundary-layer computations is presented in §§ 5 and 6 respectively. We conclude in § 7 with a short summary.

2. Second-moment closure modelling

For compressible flows it is common practice to apply Favre averaging to the Navier–Stokes equations. The Favre average of a variable ϕ is defined as

$$\tilde{\phi} = \frac{\overline{\rho\phi}}{\overline{\rho}}, \tag{2.1}$$

where ρ is the fluid density, $\overline{(\cdot)}$ denotes a Reynolds average, and $\tilde{(\cdot)}$ a Favre average. In the following ϕ' and ϕ'' denote Reynolds and Favre fluctuations respectively. The Reynolds stress tensor is given by

$$R_{ij} = \frac{\overline{\rho u_i'' u_j''}}{\overline{\rho}}. \tag{2.2}$$

Using these definitions the Favre-averaged conservation of mass, momentum and total energy equations become

$$\frac{\partial \overline{\rho}}{\partial t} + \frac{\partial}{\partial x_i}(\overline{\rho}\tilde{u}_i) = 0, \tag{2.3}$$

$$\frac{\partial}{\partial t}(\overline{\rho}\tilde{u}_i) + \frac{\partial}{\partial x_j}(\overline{\rho}\tilde{u}_i\tilde{u}_j) = -\frac{\partial \overline{p}}{\partial x_i} + \frac{\partial}{\partial x_k}\left(\overline{\sigma}_{ik} - \overline{\rho}R_{ik}\right), \tag{2.4}$$

$$\frac{\partial}{\partial t}(\overline{\rho}E) + \frac{\partial}{\partial x_i}(\overline{\rho}\tilde{u}_i H) = \frac{\partial}{\partial x_j}\left[-q_{L_j} - \overline{\rho u_j'' h''} + \overline{\sigma_{ij}u_i''} - \frac{1}{2}\overline{\rho u_i'' u_i'' u_j''} + \tilde{u}_i\left(\overline{\sigma}_{ij} - \overline{\rho}R_{ij}\right)\right], \tag{2.5}$$

where $\overline{p}$ is the average pressure, E total energy, H total enthalpy, $\overline{\sigma}_{ij}$ the viscous stress tensor, and q_{L_j} the molecular heat flux vector. The total energy and enthalpy are given by

$$E = \tilde{e} + \frac{\tilde{u}_i \tilde{u}_i}{2} + k, \quad H = \tilde{h} + \frac{\tilde{u}_i \tilde{u}_i}{2} + k, \tag{2.6}$$

where $\tilde{e}$ is the specific internal energy, $\tilde{h}$ specific enthalpy and $k = R_{ii}/2$ turbulent kinetic energy. For a Newtonian fluid, the viscous stress tensor is

$$\sigma_{ij} = \mu \left(\frac{\partial u_i}{\partial x_j} + \frac{\partial u_j}{\partial x_i} \right) - \frac{2}{3} \mu \frac{\partial u_k}{\partial x_k} \delta_{ij}, \quad \delta_{ij} = \begin{cases} 1 & \text{if } i = j, \\ 0 & \text{otherwise,} \end{cases} \tag{2.7}$$

where μ is the molecular viscosity, and δ_{ij} the Kronecker delta tensor. The molecular heat flux vector is

$$q_{L_j} = -\kappa \frac{\partial \tilde{T}}{\partial x_j}, \tag{2.8}$$

where κ is the thermal conductivity, and $\tilde{T}$ temperature. The focus of this paper is on modelling pressure effects in the Reynolds stress equation. For the sake of completeness, we first briefly discuss models for the other unclosed terms.

2.1. *Energy equation closures*

As indicated in the introduction, this work focuses only on pressure-related phenomena. Here we merely indicate the simplest energy equation closures in the literature. The correlation between fluctuating velocity and fluctuating specific enthalpy is the turbulent heat transfer and is usually modelled as

$$q_{T_j} = \overline{\rho u_j'' h''} = -\frac{c_p \mu_t}{Pr_t} \frac{\partial \tilde{T}}{\partial x_j}, \tag{2.9}$$

where Pr_t is the turbulent Prandtl number, μ_t is the turbulent viscosity, and c_p is the specific heat at constant pressure. The turbulent viscosity is computed using

$$\mu_t = \frac{\overline{\rho} C_\mu k^2}{\varepsilon}, \quad k = \frac{1}{2} R_{ii}, \quad \varepsilon = \frac{1}{2} \varepsilon_{ii}, \tag{2.10}$$

where k is the turbulent kinetic energy, and ε the dissipation rate. The modelling constants used are

$$C_\mu = 0.09, \quad Pr_t = 0.85. \tag{2.11}$$

An algebraic closure model for the turbulent heat flux in high-speed shear flows has been developed by Bowersox (2009), and used to predict velocity and temperature profiles of supersonic and hypersonic boundary layers with high accuracy. Bowersox (2009) shows that large improvements in near-wall predictions can be made by using a sophisticated turbulent heat flux model and accounting for variable Pr_t effects.

The two terms $\overline{\sigma_{ij} u_i''}$ and $\overline{\rho u_i'' u_i'' u_j''}/2$ on the right-hand side of (2.5) are the molecular diffusion and turbulent transport of turbulence kinetic energy. If $\overline{\rho} k \ll \overline{p}$, these terms can be neglected, Wilcox (1993). However, for hypersonic flows these terms may be important, and the following approximation has been suggested:

$$\overline{\sigma_{ij} u_i''} - \frac{1}{2} \overline{\rho u_i'' u_i'' u_j''} = \left(\mu + \frac{\mu_t}{\sigma_k} \right) \frac{\partial k}{\partial x_j}, \quad \sigma_k = 0.82. \tag{2.12}$$

Introducing equations (2.9) and (2.12) in equation (2.5) yields the modelled total energy equation

$$\frac{\partial}{\partial t}(\overline{\rho}E) + \frac{\partial}{\partial x_i}(\overline{\rho}\tilde{u}_i H) = \frac{\partial}{\partial x_j}\left[\left(\kappa + \frac{c_p \mu_t}{Pr_t}\right)\frac{\partial \tilde{T}}{\partial x_j} + \left(\mu + \frac{\mu_t}{\sigma_k}\right)\frac{\partial k}{\partial x_j} + \tilde{u}_i\left(\overline{\sigma}_{ij} - \overline{\rho}R_{ij}\right)\right]. \tag{2.13}$$

2.2. *Reynolds stress closures*

The Favre-averaged Reynolds stress equation takes the following form:

$$\frac{\partial\left(\overline{\rho}R_{ij}\right)}{\partial t} + \frac{\partial\left(\overline{\rho}\tilde{u}_k R_{ij}\right)}{\partial x_k} = \overline{\rho}\left(P_{ij} - \varepsilon_{ij}\right) - \frac{\partial T_{ijk}}{\partial x_k} + \Pi_{ij} + \Sigma_{ij}, \tag{2.14}$$

where P_{ij} is the production tensor, ε_{ij} the dissipation tensor, T_{ijk} the turbulent transport tensor, Π_{ij} the pressure–strain correlation, and Σ_{ij} the mass-flux coupling tensor. Of the five terms on the right-hand side of (2.14), the production tensor is the only one in closed form:

$$P_{ij} = -R_{ik}\frac{\partial \tilde{u}_j}{\partial x_k} - R_{jk}\frac{\partial \tilde{u}_i}{\partial x_k}. \tag{2.15}$$

The remaining four phenomena require closure modelling:

$$\varepsilon_{ij} = \frac{1}{\overline{\rho}}\left(\overline{\sigma'_{jk}\frac{\partial u''_i}{\partial x_k} + \sigma'_{ik}\frac{\partial u''_j}{\partial x_k}}\right), \tag{2.16}$$

$$T_{ijk} = \overline{\rho u''_i u''_j u''_k} + \overline{p' u''_i}\delta_{jk} + \overline{p' u''_j}\delta_{ik} - \overline{\sigma'_{jk}u''_i} - \overline{\sigma'_{ik}u''_j}, \tag{2.17}$$

$$\Pi_{ij} = \overline{p'\left(\frac{\partial u''_i}{\partial x_j} + \frac{\partial u''_j}{\partial x_i}\right)}, \tag{2.18}$$

and

$$\Sigma_{ij} = \overline{u''_i}\left(\frac{\partial \overline{\sigma}_{jk}}{\partial x_k} - \frac{\partial \overline{p}}{\partial x_j}\right) + \overline{u''_j}\left(\frac{\partial \overline{\sigma}_{ik}}{\partial x_k} - \frac{\partial \overline{p}}{\partial x_i}\right). \tag{2.19}$$

2.2.1. *Turbulent transport*

High-speed compressible mixing-layer simulations of Vreman, Sandham & Luo (1996), Freund *et al.* (2000) and Pantano & Sarkar (2002) clearly show that with increasing Mach number dissipation rate remains nearly the same even as production and turbulent transport decrease in absolute value across the entire mixing layer. Among the two critical turbulent transport components, pressure transport is small compared to triple velocity correlation transport and becomes smaller with increasing Mach number. Vreman *et al.* (1996) further point out that dilatational dissipation and pressure–dilatation are not large at high Mach numbers even in the presence of eddy shocklets. All three studies clearly show that the reduction in shear-layer growth rate is directly attributable to the pressure–strain correlation term. The transport tensor is modelled using the traditional scalar turbulent diffusivity approach (Lien & Leschziner 1994):

$$-\frac{\partial T_{ijk}}{\partial x_k} = \frac{\partial}{\partial x_k}\left[\left(\mu + \frac{\mu_t}{\sigma_k}\right)\frac{\partial R_{ij}}{\partial x_k}\right]. \tag{2.20}$$

It is important that this closure be consistent with the energy flux model in (2.12). It is quite possible that μ_t may be a function of the Reynolds number. However, there

is no clear experimental evidence at this time. With this closure, the reduction in turbulent transport with increasing Mach number is achieved via a reduction in μ_t due to reduced levels of turbulent kinetic energy.

2.2.2. *Dissipation tensor*

It is suggested in the literature that the smallest scales of motion are likely to be isotropic even at reasonably large Mach numbers. This is due to the fact that Mach-number effects are less significant at small scales as the characteristic velocity diminishes with scale. Consequently, the Mach number characterizing the smallest scales of motion is small in many flows of interest. Thus, the isotropic model is assumed to remain valid for the dissipation tensor

$$\varepsilon_{ij} = \tfrac{2}{3}\varepsilon\delta_{ij}. \tag{2.21}$$

As in incompressible turbulence, a model evolution equation must be solved to find the turbulent dissipation rate ε. In all closure models to date, the dissipation rate is taken to be the spectral cascade rate. The spectral cascade rate equation must be enhanced to include the effect of compressibility. Furthermore, the influence of variation in transport coefficient μ on dissipation must be understood and modelled. We address these issues in detail in the next section.

2.2.3. *Turbulent mass flux*

DNS of supersonic shear layers (Pantano & Sarkar 2002) has shown the mass flux coupling term Σ_{ij} to be negligible in the Reynolds stress budgets. Since it is our intention to propose a model that can capture the compressibility effects associated with high-speed boundary and mixing layers, it is reasonable to neglect this term. However, for flows driven by density gradients, this term is of paramount importance (Livescu & Ristorcelli 2007, 2008). For such flows, Ristorcelli (1993) presents an algebraic turbulent mass-flux model.

2.2.4. *Pressure-effects closures*

The fluctuating pressure equation for compressible flows has been analysed by Thacker, Sarkar & Gatski (2007),

$$\left[\frac{1}{a^2}\left(\frac{\partial}{\partial t}+\tilde{u}_j\frac{\partial}{\partial x_j}\right)^2-\frac{\partial^2}{\partial x_j\partial x_j}\right]p' = \left\{\frac{\partial^2}{\partial x_i\partial x_j}(\rho u_i''u_j''-\overline{\rho}R_{ij})\right\}$$
$$+\left\{2\frac{\partial\tilde{u}_i}{\partial x_j}\frac{\partial\left(\rho u_j''\right)}{\partial x_i}+\rho'\frac{\partial\tilde{u}_i}{\partial x_j}\frac{\partial\tilde{u}_j}{\partial x_i}+\left(\frac{\partial}{\partial t}+\tilde{u}_j\frac{\partial}{\partial x_j}\right)\tilde{u}_i\frac{\partial p'}{\partial x_i}\right\}. \tag{2.22}$$

The first set of terms within curly braces on the right-hand side arises due to the 'slow' pressure, which is nonlinear in the fluctuating velocity. Its response to changes in the mean velocity field is slow due to modifications of the fluctuating velocity field occurring over longer time periods compared to mean velocity field modifications. The second set of terms within curly braces on the right-hand side of (2.22) is due to 'rapid' pressure and is linear in the fluctuating velocity field. The adjective rapid comes from the fact that this portion of the pressure field reacts rapidly upon a change in the mean flow. The linear part captures the interaction between mean and fluctuating fields while the nonlinear part accounts for interactions among fluctuating fields. Thacker *et al.* (2007) provide a detailed discussion of the fluctuating pressure equation in the context of supersonic mixing and boundary layers.

Classical pressure–strain correlation modelling methodology (Speziale *et al.* 1991) commences from the following form:

$$\Pi_{ij} = \overline{\rho}\varepsilon \mathscr{A}_{ij}(\boldsymbol{b}) + \overline{\rho} k \mathscr{M}_{ijkl}(\boldsymbol{b}) \frac{\partial \tilde{u}_k}{\partial x_l}, \tag{2.23}$$

where

$$b_{ij} \equiv \frac{R_{ij}}{2k} - \frac{1}{3}\delta_{ij} \tag{2.24}$$

is the anisotropy tensor. Corresponding to slow and rapid pressure, the pressure–strain correlation is also decomposed into its slow and rapid parts:

$$\Pi_{ij} = \Pi_{ij}^{(s)} + \Pi_{ij}^{(r)}, \quad \Pi_{ij}^{(s)} = \overline{\rho}\varepsilon \mathscr{A}_{ij}(\boldsymbol{b}), \quad \Pi_{ij}^{(r)} = \overline{\rho} k \mathscr{M}_{ijkl}(\boldsymbol{b}) \frac{\partial \tilde{u}_k}{\partial x_l}. \tag{2.25}$$

Dimensional analysis and representation theory (Smith 1971; Pennisi & Trovato 1987) of tensor-valued isotropic functions allows the pressure–strain correlation to be written as

$$\Pi_{ij} = \overline{\rho}\varepsilon f_{ij}(\boldsymbol{b}, \tau \boldsymbol{S}, \tau \boldsymbol{W}) = \overline{\rho}\varepsilon \sum_k C_k T_{ij}^k, \quad \tau = \frac{k}{\varepsilon}, \tag{2.26}$$

where

$$S_{ij} = \frac{1}{2}\left(\frac{\partial \tilde{u}_i}{\partial x_j} + \frac{\partial \tilde{u}_j}{\partial x_i}\right) - \frac{1}{3}\frac{\partial \tilde{u}_k}{\partial x_k}\delta_{ij}, \quad W_{ij} = \frac{1}{2}\left(\frac{\partial \tilde{u}_i}{\partial x_j} - \frac{\partial \tilde{u}_j}{\partial x_i}\right) \tag{2.27}$$

are the modified rate-of-strain and rotation-rate tensors respectively. The C_k coefficients in (2.26) are in general scalar functions of the independent tensor invariants of the tensor-valued isotropic functions (T_{ij}^k). Nonetheless many popular models use constant values for some or all of these coefficients (Launder *et al.* 1975; Jones & Musonge 1988; Speziale *et al.* 1991). The final compressibility effect that requires special consideration is pressure–dilatation. This effect is absent in incompressible flows but plays the vital role of transferring energy between internal and dilatational kinetic energies in compressible flows. Closure models for the pressure–strain correlation, pressure–dilatation, and dissipation rate are the focus of the next section.

3. Compressible shear turbulence: physics and closure modelling

The fundamental physics of flow–thermodynamic interactions that leads to stabilization of turbulence has been investigated and reported in three preceding works from our research group: Lavin *et al.* (2012), Lee & Girimaji (2013) and Bertsch *et al.* (2012). The linear aspects of flow stabilization that are generic to compressible shear flows have been examined in Lavin *et al.* (2012) using RDT. Pressure–strain correlation model implications are investigated in Bertsch *et al.* (2012). The nonlinear aspects of the pressure–strain correlation are studied in Lee & Girimaji (2013) wherein the slow pressure physics are established. All of these findings form the basis of the model development in this study. Thus, the present paper represents the culmination of a series of studies directed towards understanding fundamental compressible shear flow physics and incorporating them into closure models using sound first principles. In this section we present the known physics of compressible shear turbulence and proceed to propose closure models. Following the incompressible turbulence precedent, we

separate the linear and nonlinear physics effects as they represent distinctly different aspects of turbulence dynamics. The focus is on the pressure–strain correlation term and its consequences on pressure–dilatation and spectral cascade rate.

The dimensionless parameters of relevance are the gradient Mach number (M_g) and turbulent Mach number (M_t) defined as

$$M_g \equiv \frac{Sl}{a}, \quad M_t \equiv \frac{\sqrt{2k}}{a}. \tag{3.1}$$

The gradient Mach number is the ratio of shear to acoustic time scale, whereas the turbulent Mach number characterizes the magnitude of velocity fluctuations relative to speed of sound. The relative magnitudes of the mean-flow distortion time scale ($\tau_d = 1/S$), and acoustic time scale ($\tau_a = l/a$) determine the magnitude of the gradient Mach number ($M_g = \tau_a/\tau_d$). In hypersonic flows of aerospace engineering interest, gradient Mach numbers can be much larger than unity. However, turbulent Mach numbers are typically smaller than unity. In the model development phase, we restrict ourselves to a parameter range of practical utility in hypersonic flight vehicles: gradient Mach numbers up to 10 and turbulence Mach numbers less than 0.6.

3.1. *Linear pressure–strain correlation*

As mentioned in the previous section, linear or rapid pressure corresponds to the fluctuating pressure field that arises due to the presence of the mean velocity gradient. In the rapid distortion limit, this is the only pressure fluctuation of relevance. It stands to reason that the parameterization of linear pressure–strain correlation involves the mean-flow parameters. Compressible rapid distortion theory studies have shown that the linear pressure–strain correlation is profoundly affected by compressibility (Cambon *et al.* 1993; Simone *et al.* 1997; Livescu & Madnia 2004; Bertsch 2010; Lavin *et al.* 2012). The study by Simone *et al.* (1997) suggests that the rapid or linear pressure is chiefly responsible for the reduction of turbulent kinetic energy growth rates in compressible homogeneous shear at high gradient Mach number. The implication for modelling is that critical changes to the incompressible rapid pressure–strain correlation closure are needed for applicability in compressible flows. Furthermore, these changes should be parameterized by the gradient Mach number (Durbin & Zeman 1992; Cambon *et al.* 1993; Lavin *et al.* 2012).

We commence from the findings of the rapid distortion studies of compressible homogeneous shear flow performed by Bertsch (2010) and Lavin *et al.* (2012). Figures 2 and 3 show the turbulent kinetic energy evolution in acoustic and shear time respectively. From figure 2 a three-stage behaviour in the growth rate of turbulent kinetic energy can be observed. This three-stage behaviour can be used to establish a fundamental guideline for the effect of pressure at low, intermediate, and high gradient Mach number.

Regime 1: $M_g \gg 1$, $\tau_a \gg \tau_d$. In this regime the acoustic time scale is much larger than that of shear. Pressure responds too slowly to affect the flow dynamics. As a result, turbulence evolution is dominated by the production process

$$\Pi_{ij} \ll P_{ij}. \tag{3.2}$$

This regime is characterized by minimal flow–thermodynamics interactions as well as high levels of Reynolds stress anisotropy. The turbulent kinetic energy growth rate in the pressure-released stage increases with initial gradient Mach number, as can be seen for $St < 2$ in figure 3. In this limit, the flow evolution

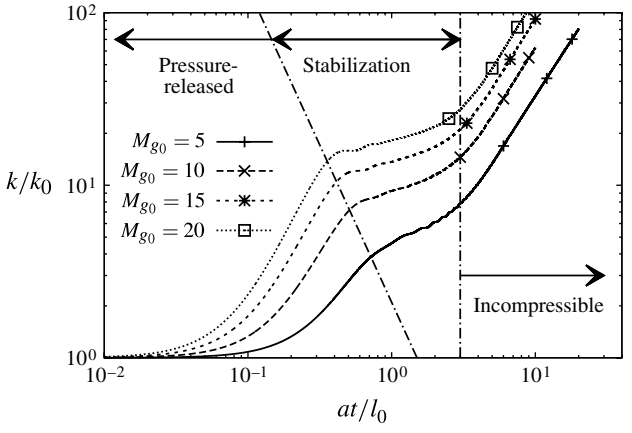

FIGURE 2. Turbulent kinetic energy evolution in acoustic time. RDT of compressible homogeneous shear flow, taken from Bertsch (2010).

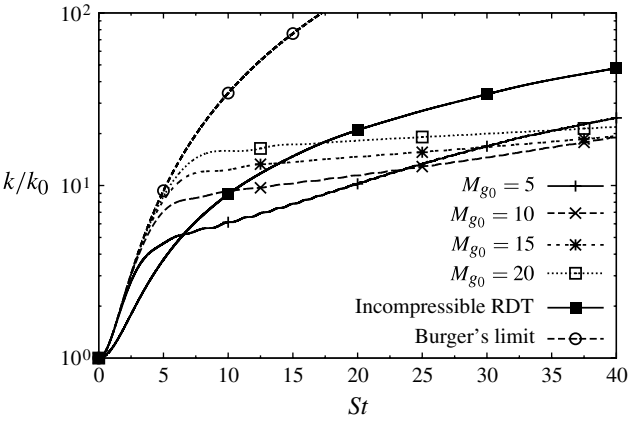

FIGURE 3. Turbulent kinetic energy evolution in shear time, St, which is defined in (3.12). RDT of compressible homogeneous shear flow, taken from Bertsch (2010).

can be closely approximated by the three-dimensional Burgers equation, which is the Navier–Stokes equation without the pressure term (Bertsch *et al.* 2012).

Regime 2: $M_g \sim 1$, $\tau_a \sim \tau_d$. This flow regime occurs when the mean distortion and acoustic time scales are of similar magnitude. In this stage both inertial and pressure effects play critical roles. The acoustic character of the pressure field is most evident in this regime. Pressure waves are established in the flow normal (shear) direction. This leads to oscillatory behaviour of shear normal velocity fluctuations (Lavin *et al.* 2012). Consequently the fluctuating shear stress also evolves in an oscillatory manner as shown by Bertsch (2010) and Lavin *et al.* (2012). The small integrated value of R_{12} in this stage results in a negligible net growth of turbulent kinetic energy as seen in figure 2. During this stabilization stage Bertsch (2010) demonstrates that on an average

$$\Pi_{12}^{(r)} + P_{12} \approx 0. \tag{3.3}$$

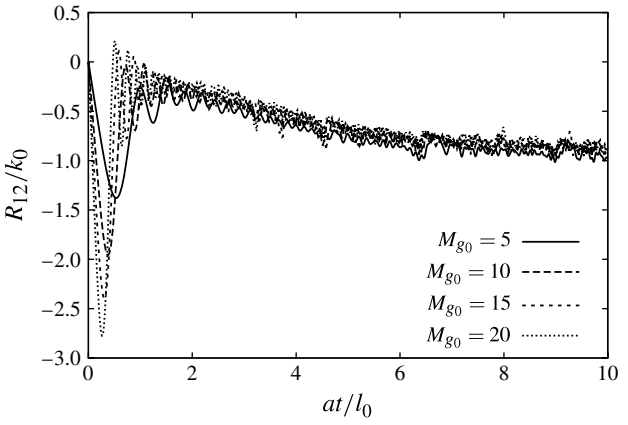

FIGURE 4. Normalized Reynolds shear stress evolution in acoustic time. RDT of compressible homogeneous shear flow, taken from Bertsch (2010).

This regime has the highest level of flow–thermodynamics interactions, leading to maximum energy exchange between turbulent kinetic and potential forms. The spectral cascade rate is affected the most in this regime. Anisotropy is moderate and flow stabilization is incipient. Based on these observations, we suggest that shear production blocking by the corresponding pressure–strain correlation component is the critical aspect of flow physics that must be incorporated into compressible closure models.

Regime 3: $M_g \ll 1$, $\tau_a \ll \tau_d$. At low gradient Mach number, pressure assumes the role of enforcing incompressibility and is governed by a Poisson equation. Pressure equilibrates almost instantaneously to inertial effects and maintains incompressibility. Any remnant dilatational fluctuations are rapidly dissipated by viscous effects. For this low-M_g regime, a standard incompressible pressure–strain correlation model is taken to be adequate:

$$\Pi_{ij} \approx \Pi_{ij}^{I}. \tag{3.4}$$

This regime is characterized by negligible flow–thermodynamics interactions with low levels of anisotropy and no flow stabilization. In this regime, the turbulent kinetic energy growth rates for all cases are reasonably similar to that of low gradient Mach number, as seen in figure 2. The RDT computations of Bertsch (2010) demonstrate that for this stage the normalized shear Reynolds stress goes to an approximately constant value independent of initial gradient Mach number, as seen for large acoustic time in figure 4.

The three-stage behaviour described here is consistent with the three regimes of compressible shear flows analysed in Livescu & Madnia (2004). There the three regimes are called: (i) pressure-released; (ii) incompressible; and (iii) intermediate-time. The authors analyse the compressible RDT equations and establish the existence of two regions of wavenumbers in spectral space: inner and outer regions. The inner region consists of wavenumbers in the close proximity of the spanwise direction and the outer region is made up of all other wavenumbers. It is clearly established that at late times, the wavenumbers in the inner region contribute most to the kinetic energy in both incompressible and compressible shear turbulence. The velocity field generated

by the inner wavenumber is predominantly solenoidal in nature at all speeds. Most of the dilatational field statistics and higher-order structure functions receive the majority of their contributions from the outer regions. Livescu & Madnia (2004) go on to show that the outer regime of wavenumbers contributes mostly to the pressure-released and finite-time limits. Bertsch *et al.* (2012) demonstrate that independent of Mach number, at late times the solenoidal fluctuations contain almost 90 % of the turbulent kinetic energy. Thus for this late stage the velocity field can be considered approximately incompressible.

Overall, the three-stage behaviour described in Lavin *et al.* (2012) and Bertsch *et al.* (2012) is completely consistent with the analysis of Livescu & Madnia (2004). Therefore, such a three-stage paradigm is a reasonable basis upon which the linear (rapid) pressure–strain correlation can be developed.

Closure modelling of the linear pressure–strain correlation. In summary, Lavin *et al.* (2012) conclude that dilatational fluctuations dominate the flow physics in Regimes 1 and 2 whereas solenoidal fluctuations dominate in Regime 3. Residual dilatations may exist in Regime 3 but as a modelling simplification can be taken to be small and perhaps negligible. Thus motivated we propose a compressible pressure–strain correlation of the following general form: (Pope 2000)

$$\Pi_{ij}^{(r)} = \overline{\rho}\varepsilon \sum_k C_k\left(M_g\right) T_{ij}^{k(r)} - \overline{\rho} C_P\left(M_g\right) P_{ij}. \tag{3.5}$$

For the sake of generality, the coefficients are functions of gradient Mach number. The addition of the production-blocking term does not violate form invariance since the production tensor can be expressed as a sum of tensor-valued isotropic functions. The production-blocking term is clearly motivated by the behaviour observed in Regime 2 as described above. On the other hand, the dependence of the coefficients on Mach number is to accommodate Regime 1 behaviour, wherein the effect of the pressure–strain correlation gradually fades with increasing Mach number.

We use the same tensor groups in the rapid pressure–strain correlation as those found in the incompressible LRR model (Launder *et al.* 1975):

$$\begin{aligned}\Pi_{ij}^{(r)} = {} & C_3\left(M_g\right)\overline{\rho}kS_{ij} + C_4\left(M_g\right)\overline{\rho}k\left(b_{ik}S_{jk} + b_{jk}S_{ik} - \tfrac{2}{3}b_{mn}S_{mn}\delta_{ij}\right) \\ & + C_5\left(M_g\right)\overline{\rho}k\left(b_{ik}W_{jk} + b_{jk}W_{ik}\right) - C_P\left(M_g\right)\overline{\rho}P_{ij}.\end{aligned} \tag{3.6}$$

The linearity of (3.6) permits a straightforward implementation to the standard explicit algebraic Reynolds stress model (EARSM) approach (Girimaji 1996), a concurrent undertaking to the present modelling efforts.

Some treatments of compressible flows partition the fluctuating velocity field into solenoidal (vortical) and dilatational (acoustic) fields. Dilatational effects are relevant at high Mach numbers in the pressure-released and stabilization regimes. The solenoidal velocity and pressure fields play the dominant role in the incompressible regime. In this work, we do not distinguish explicitly between the two types of fluctuations. As mentioned earlier, the two different physical effects are implicit in the nature of the closure in the three stages. Rather, we focus on model development in the three regimes identified from the RDT study. It is found that Regimes 1 and 2 are dominated by dilatational fluctuations as the pressure does not effectively impose the divergence-free condition on the velocity gradient field. In Regime 3, the solenoidal aspects are the most important. Thus, the dilatational and solenoidal aspects of flow physics are naturally incorporated in this approach in the appropriate parameter regimes.

3.2. *Nonlinear pressure–strain correlation*

Lee & Girimaji (2013) performed a DNS study of decaying anisotropic compressible turbulence for a range of turbulent Mach numbers and temperature fluctuations. This study isolates the effects that compressibility and thermodynamic fluctuations have on the nonlinear pressure–strain correlation in the limit of decaying turbulence. Lee & Girimaji (2013) conclude that the return to isotropy of the solenoidal kinetic energy k_s is largely unaffected for moderate turbulent Mach number ($M_t \leqslant 0.6$), and temperature fluctuations ($T'_{rms}/\overline{T} \leqslant 0.27$). On the other hand, the dilatational kinetic energy k_d is affected by both turbulent Mach number and temperature fluctuations. However the total kinetic energy field returns to isotropy at approximately the same rate for the entire parameter range in the study. Therefore, as long as the flows of interest are within the turbulent Mach number and temperature fluctuation parameter range examined in the study, we can use the same the form of the slow incompressible pressure–strain correlation for compressible flows. However, this does not preclude modifications to the slow pressure–strain correlation model at higher turbulent Mach number.

Closure modelling of the nonlinear pressure–strain correlation. Based on the findings above, the Rotta (1951) model is chosen for the slow pressure–strain correlation:

$$\Pi_{ij}^{(s)} = -C_1\left(M_t\right)\overline{\rho}\varepsilon b_{ij}. \tag{3.7}$$

The dependence on M_t reflects the degree of influence of dilatational fluctuations. The modification can be expected to be higher at larger M_t due to a greater fraction of dilatational fluctuations. The complete pressure–strain correlation model is given by the sum of (3.6) and (3.7). In the following, for notational convenience we refrain from explicitly showing the dependence of the C_k and C_P coefficients on M_g.

3.3. *Linear pressure–dilatation*

Sarkar, Erlebacher & Hussaini (1991*b*) and Lavin *et al.* (2012) report that the linear pressure–dilatation acts to bring about equipartition between dilatational kinetic energy and turbulent internal energy. In homogeneous shear flow without heat release, the net energy transfer is from kinetic to internal form. This is the most fundamental interaction pressure–dilatation can cause, and should at a minimum be the basis for pressure–dilatation modelling.

Closure modelling of the linear pressure–dilatation. The trace of equation (3.5) leads to the following linear pressure–dilatation model:

$$\frac{1}{2}\Pi_{ii}^{(r)} = -\overline{\rho}C_P\left(M_g\right)P = \overline{\rho}kC_P\left(M_g\right)\left(2b_{mn}S_{mn} + \frac{2}{3}\frac{\partial\tilde{u}_m}{\partial x_m}\right), \quad P = \frac{1}{2}P_{ii}. \tag{3.8}$$

For positive C_P, the above model guarantees that for shear-dominated flows in the absence of heat release the net transfer of energy is from kinetic to internal, as observed in DNS.

3.4. *Nonlinear pressure–dilatation*

Closure modelling of the nonlinear pressure–dilatation. In the cases of interest here, the slow term is expected to be negligible and hence a nonlinear pressure–dilatation model is not used in the calibration or computations:

$$\Pi^{(s)} = \tfrac{1}{2}\Pi_{ii}^{(s)} = 0. \tag{3.9}$$

3.5. *Dissipation rate*

Closure modelling of dissipation in compressible flows entails consideration of three novel aspects absent in incompressible flows: (i) dilatational dissipation; (ii) the effect of large viscosity gradients on solenoidal dissipation; and (iii) inviscid passage of energy from kinetic to internal (due to pressure–dilatation) and thus by-passing the spectral cascade. In the following, each point is discussed individually.

It is now commonly accepted (Smits & Dussauge 2006) that in the absence of heat release, the dilatational to solenoidal dissipation ratio scales as

$$\varepsilon_d/\varepsilon_s \sim M_t^4. \tag{3.10}$$

Livescu *et al.* (2002) show that for compressible homogeneous shear without heat release, dilatational dissipation is small compared to solenoidal dissipation. However the magnitude of dilatational dissipation can be strongly magnified by intense heat release. Lee & Girimaji (2013) estimate that the extent of dilatational kinetic energy is proportional to the pressure fluctuation induced by heat release. It is clear that the presence of significant heat release can severely complicate the energetic turbulence dynamics. The development of an all-encompassing model is beyond the scope of the current work. Instead, as a first step, we focus on non-reacting compressible turbulence with moderate turbulent Mach number, and thermodynamic fluctuations. For the parameter range of interest, $M_t \leqslant 0.6$, the effect of compressible dissipation can be neglected.

Due to the high degree of interactions between momentum, energy, and state equations in compressible flow, large gradients of temperature and therefore viscosity can be expected. Under these circumstances, the validity of Taylor's postulate that dissipation rate is independent of viscosity at high Reynolds number can come into question. Lee, Girimaji & Kerimo (2008) use DNS to examine if Taylor's postulate holds true in a variable-viscosity medium. They find that the velocity gradients rapidly adapt to the viscosity field, and within half an eddy turnover time, the dissipation rate becomes independent of viscosity. Thus as a first approximation, we can expect that even in the presence of large gradients of viscosity, Taylor's postulate is valid after a brief initial transient period.

For non-reacting compressible homogeneous shear, pressure–dilatation transfers turbulent kinetic energy to turbulent internal energy. This energy transfer can potentially affect the dissipation rate equation. In the standard incompressible dissipation rate model, the spectral cascade rate is taken to be equal to the dissipation rate. However for compressible flows, the energy transferred by pressure–dilatation does not cascade down to smaller scales as the spectral energy flux. In this work, we attempt to determine if this reduction in the cascade rate must be incorporated into the closure model.

Closure modelling of dissipation. We present a turbulent dissipation rate equation that is suitably modified from its standard form to allow for the effect of pressure–dilatation:

$$\frac{\partial}{\partial t}(\overline{\rho}\varepsilon) + \frac{\partial}{\partial x_i}(\overline{\rho}\varepsilon\tilde{u}_i) = \frac{\partial}{\partial x_j}\left[\left(\mu + \frac{\mu_t}{\sigma_\varepsilon}\right)\frac{\partial \varepsilon}{\partial x_j}\right] + C_{\varepsilon_1}\overline{\rho}\frac{\varepsilon}{k}P\,(1 - C_P) - C_{\varepsilon_2}\overline{\rho}\frac{\varepsilon^2}{k}. \tag{3.11}$$

The overall effect of including C_P in the dissipation rate equation is to reduce the production of dissipation. To assess the impact of cascade by-pass, we present two closure proposals for the dissipation equation: closure GG-I uses the standard

dissipation rate equation (equation (3.11) without the C_P term) and closure GG-II includes the proposed modification.

3.6. *Choice of length scale*

The most appropriate length scale for use in the gradient Mach number definition is the characteristic acoustic length scale. Sarkar (1995) characterizes this as the representative length scale in the shear direction. Lavin *et al.* (2012) show that the acoustic component is dominant in the shear direction and hence Sarkar (1995) and Lavin *et al.* (2012) are consistent with one another. Such a length scale can also be of use in modelling dilatational dissipation. However, in the traditional second-moment approach the only length scale available is the integral scale given by $l = k^{3/2}/\varepsilon$. Two possible options for obtaining the requisite acoustic length scale are: (i) solve a modelled evolution equation for the acoustic length scale; and (ii) relate the acoustic length scale to the integral length scale by suitable calibration. Development of a new modelled evolution equation for the acoustic length scale, while highly desirable, is the more difficult of the two options. Such an equation is likely to be even more empirical than the incompressible length scale equation, and would represent a major paradigm shift. In this work, we opt for the simpler alternative and defer the development of an acoustic length scale equation to the future. Thus, in our work we characterize compressibility effects using a gradient Mach number that utilizes $l = k^{3/2}/\varepsilon$ as the length scale. Any difference between the acoustic and integral length scales is accounted for in the calibration process. With this choice of length scale, the gradient and turbulent Mach numbers are related. Therefore we use the gradient Mach number as the only compressible parameter in the fixed-point analysis. The gradient Mach number is found using

$$M_g \equiv \frac{Sl}{a}, \quad S = \sqrt{2S_{ij}S_{ij}}, \quad l = \frac{k^{3/2}}{\varepsilon}, \quad a = \sqrt{\gamma R\tilde{T}}, \quad \frac{M_t}{M_g} = \sqrt{2}\left(\frac{Sk}{\varepsilon}\right)^{-1}. \tag{3.12}$$

Now that the model forms of the unclosed terms have been established, we proceed to develop a validation road map using fixed-point analysis.

4. Fixed-point analysis

Fixed-point and dynamical system analysis have long been used for incompressible turbulence closure model development (Speziale *et al.* 1991, 1992; Girimaji 2000). Analytical relationships between model coefficients and asymptotic behaviour can be derived for homogeneous flows. In Girimaji (2000) it is argued that demanding that the model coefficients yield the correct asymptotic self-similar turbulence state is an effective closure model development strategy. Here we extend that approach to compressible flows. As the focus of this work is shear-dominated flows, we determine the closure coefficients by matching model fixed-point behaviour to DNS asymptotic Reynolds stress anisotropy values at various gradient Mach numbers. We show how this approach leads to reasonable agreement with the temporal evolution of compressible homogeneous shear DNS.

4.1. *Incompressible flow*

Detailed methodology for utilizing fixed-point analysis for incompressible second-moment closure is given in Girimaji (2000). Here we provide a brief synopsis before extending it to compressible flows. From a given initial state parameterized by mean strain and rotation rate, kinetic energy and dissipation, a homogeneous turbulence field

evolves toward an asymptotic state where appropriately normalized turbulence field variables approach an invariant state. In incompressible turbulence the key parameters that characterize the initial state of turbulence are normalized strain, Sk/ε, and rotation, $\Omega k/\varepsilon$, rates. The specific initial values of k, ε, and anisotropic state are less important. The normalized field variables that characterize the fixed-point asymptotic state are anisotropy components b_{ij}, and production to dissipation ratio P/ε. This cause–effect relationship is used to determine the unknown coefficients in the pressure–strain correlation closure. In other words, the closure model coefficients are chosen to yield the correct asymptotic state for a given initial strain/rotation tensor combination. In inhomogeneous unsteady calculations, mean strain and rotation rates change in time and space. The closure model temporally advances the computed solution toward the fixed point corresponding to the current strain and rotation rate tensors. As these tensors change in space and time, the evolution trajectory will change correspondingly. This approach has led to successful calibration of incompressible turbulence closure models (Speziale *et al.* 1991; Girimaji 2000).

4.2. *Extension to compressible flow*

The fixed-point calibration rationale should in principle also apply for compressible turbulence closure models. The main challenge is to identify novel parameters that characterize the initial state as well as additional fixed-point characteristics appropriate for compressible turbulence. Beyond the incompressible turbulence parameters we suggest that gradient Mach number and turbulent Mach number are the key new causal parameters that must be accounted for in modelling compressibility effects. The additional asymptotic state variable that characterizes the compressibility effect is (Sarkar 1995)

$$X_\varepsilon = \frac{\overline{\rho}\varepsilon - \Pi}{\overline{\rho}P}. \tag{4.1}$$

This is the key compressible turbulence characteristic for the following reasons:

(*a*) Π accounts for energy exchange between compressible and incompressible turbulence;

(*b*) the stabilizing effect of compressibility is also manifested via production, P;

(*c*) the effect of compressibility on energy cascade rate is represented via ε.

Furthermore, the modification to turbulence anisotropy is reflected in the variation of b_{ij} with Mach number. The choice of b_{ij}, P/ε, and X_ε as the asymptotic characteristics addresses all of the physical effects of relevance. In summary, the parameters (causes) of a compressible closure are normalized initial mean strain rate and rotation rate tensors, gradient Mach number, and turbulent Mach number. The asymptotic state variables of relevance (effects) are b_{ij}, P/ε, and X_ε. The causal parameters and effects in incompressible and compressible flows are shown in table 1.

The asymptotic states can be written in a general fashion as (Speziale *et al.* 1991)

$$b_{ij_\infty} = f_{ij}\left(Sk/\varepsilon, \Omega k/\varepsilon, M_g, M_t\right), \tag{4.2}$$

$$\left(\frac{P}{\varepsilon}\right)_\infty = g\left(Sk/\varepsilon, \Omega k/\varepsilon, M_g, M_t\right), \tag{4.3}$$

and

$$X_{\varepsilon_\infty} = h\left(Sk/\varepsilon, \Omega k/\varepsilon, M_g, M_t\right), \tag{4.4}$$

	Causal initial parameters	Asymptotic state	Calibrated coefficients
Incompressible	Sk/ε, $\Omega k/\varepsilon$	b_{ij}, P/ε	C_1, C_3, C_4, C_5
Compressible	Sk/ε, $\Omega k/\varepsilon$, M_g, M_t	b_{ij}, P/ε, X_ε	C_1, C_3, C_4, C_5, C_P

TABLE 1. Causal parameters and effects for incompressible and compressible flows.

where the subscript ∞ refers to an asymptotic fixed-point value. In the following section it is shown that for calibration purposes (4.2)–(4.4) can be rewritten as

$$b_{ij\infty} = F_{ij}\left(C_1, C_3, C_4, C_5, C_P\right), \tag{4.5}$$

$$\left(\frac{P}{\varepsilon}\right)_\infty = G\left(C_{\varepsilon_1}, C_{\varepsilon_2}, C_P\right), \tag{4.6}$$

and

$$X_{\varepsilon\infty} = H\left(C_{\varepsilon_1}, C_{\varepsilon_2}, C_P\right). \tag{4.7}$$

By determining the C_k coefficients in (4.5)–(4.7) in terms of the causal initial parameters in (4.2)–(4.4), the desired asymptotic states can be adequately reproduced.

4.3. *Fixed-point analysis for shear flows*

In pure homogeneous shear the Reynolds stress, turbulent kinetic energy, and dissipation rate equations reduce to

$$\frac{\mathrm{d}\left(\overline{\rho}R_{ij}\right)}{\mathrm{d}t} = \overline{\rho}P_{ij} - \frac{2}{3}\overline{\rho}\varepsilon\delta_{ij} + \Pi_{ij}, \tag{4.8}$$

$$\frac{\mathrm{d}\left(\overline{\rho}k\right)}{\mathrm{d}t} = \overline{\rho}P - \overline{\rho}\varepsilon + \Pi = \overline{\rho}P\left(1 - C_P\right) - \overline{\rho}\varepsilon, \tag{4.9}$$

and

$$\frac{\mathrm{d}(\overline{\rho}\varepsilon)}{\mathrm{d}t} = C_{\varepsilon_1}\overline{\rho}\frac{\varepsilon}{k}P\left(1 - C_P\right) - C_{\varepsilon_2}\overline{\rho}\frac{\varepsilon^2}{k}. \tag{4.10}$$

The velocity gradient tensor for homogeneous shear is

$$\frac{\partial\tilde{u}_i}{\partial x_j} = S\delta_{i1}\delta_{j2}. \tag{4.11}$$

The fixed points of the anisotropy tensor are given by

$$\frac{\mathrm{d}b_{ij}}{\mathrm{d}t} \to 0. \tag{4.12}$$

Expressing (4.8) in terms of the anisotropy tensor yields

$$\overline{\rho}\frac{\mathrm{d}R_{ij}}{\mathrm{d}t} = 2\overline{\rho}\left[k\frac{\mathrm{d}b_{ij}}{\mathrm{d}t} + \left(b_{ij} + \frac{1}{3}\delta_{ij}\right)\frac{\mathrm{d}k}{\mathrm{d}t}\right] = \overline{\rho}P_{ij} - \frac{2}{3}\overline{\rho}\varepsilon\delta_{ij} + \Pi_{ij}. \tag{4.13}$$

Inserting $\mathrm{d}k/\mathrm{d}t$ from (4.9) and setting $\mathrm{d}b_{ij}/\mathrm{d}t = 0$ leads to the following algebraic system for describing the asymptotic state:

$$2\left(b_{ij} + \frac{1}{3}\delta_{ij}\right)\left[\frac{P}{\varepsilon}\left(1 - C_P\right) - 1\right] = \frac{P_{ij}}{\varepsilon} - \frac{2}{3}\delta_{ij} + \frac{\Pi_{ij}}{\overline{\rho}\varepsilon}. \tag{4.14}$$

Substitution of (4.11) into (2.15), (3.6), (3.7), and finally into (4.14) yields the following system for the fixed points of the anisotropy tensor in pure homogeneous shear:

$$2\left(b_{11}+\frac{1}{3}\right)\left[\frac{P}{\varepsilon}(1-C_P)-1\right]=\frac{-4Skb_{12}}{\varepsilon}-\frac{2}{3}+\frac{Sk}{\varepsilon}\left[-\frac{\varepsilon}{Sk}C_1b_{11}+\frac{1}{3}C_4b_{12}+C_5b_{12}+4C_Pb_{12}\right], \tag{4.15}$$

$$2\left(b_{22}+\frac{1}{3}\right)\left[\frac{P}{\varepsilon}(1-C_P)-1\right]=-\frac{2}{3}+\frac{Sk}{\varepsilon}\left[-\frac{\varepsilon}{Sk}C_1b_{22}+\frac{1}{3}C_4b_{12}-C_5b_{12}\right], \tag{4.16}$$

$$2b_{12}\left[\frac{P}{\varepsilon}(1-C_P)-1\right]=\frac{-2Sk\,(b_{22}+1/3)}{\varepsilon}+\frac{Sk}{\varepsilon}\left[-\frac{\varepsilon}{Sk}C_1b_{12}+\frac{1}{2}C_3+\frac{1}{2}C_4\,(b_{11}+b_{22})+\frac{1}{2}C_5\,(b_{22}-b_{11})+2C_P\,(b_{22}+1/3)\right]. \tag{4.17}$$

The production to dissipation ratio

$$\frac{P}{\varepsilon}=\frac{-2Skb_{12}}{\varepsilon}, \tag{4.18}$$

is used to simplify (4.15)–(4.17) and determine the fixed points of the anisotropy tensor:

$$b_{11_\infty}=\frac{(P/\varepsilon)_\infty\,(-1/12\,C_4-1/4\,C_5-2/3\,C_P+2/3)}{(P/\varepsilon)_\infty\,(1-C_P)+1/2\,C_1-1}, \tag{4.19}$$

$$b_{22_\infty}=\frac{(P/\varepsilon)_\infty\,(-1/12\,C_4+1/4\,C_5+1/3\,C_P-1/3)}{(P/\varepsilon)_\infty\,(1-C_P)+1/2\,C_1-1}, \tag{4.20}$$

$$b_{12_\infty}=-\left[\frac{b_{12}^*}{-24\left\{(P/\varepsilon)_\infty\,(1-C_P)+1/2\,C_1-1\right\}}\right]^{1/2}, \tag{4.21}$$

$$b_{12}^*=(P/\varepsilon)_\infty[3\,b_{11_\infty}(C_4-C_5)+3\,b_{22_\infty}(C_4+C_5+4\,C_P-4)+3\,C_3+4\,C_P-4]. \tag{4.22}$$

In the above the subscript ∞ refers to an asymptotic fixed-point value.

The final step is to determine the asymptotic value of the production to dissipation ratio. This ratio depends on the dissipation rate equation coefficients as well as the pressure–dilatation model. To test the effect of modifying the standard dissipation rate equation the two proposed models are calibrated separately: GG-I does not include the dissipation rate equation modification ((4.10) without the C_P term) and GG-II does include the modification. To find the fixed points of the production to dissipation ratio, we first need the fixed points of the dimensionless shear rate Sk/ε:

$$\frac{\mathrm{d}}{\mathrm{d}t}\left(\frac{Sk}{\varepsilon}\right)=\frac{S}{\varepsilon}\frac{\mathrm{d}k}{\mathrm{d}t}-\frac{Sk}{\varepsilon^2}\frac{\mathrm{d}\varepsilon}{\mathrm{d}t}=0. \tag{4.23}$$

Substituting for $\mathrm{d}k/\mathrm{d}t$ and $\mathrm{d}\varepsilon/\mathrm{d}t$ the fixed-point value of dimensionless shear for GG-I is

$$\left(\frac{Sk}{\varepsilon}\right)_\infty=\frac{1}{-2b_{12_\infty}}\frac{\left(C_{\varepsilon_2}-1\right)}{\left(C_{\varepsilon_1}-1+C_P\right)}. \tag{4.24}$$

Similarly, by using the GG-II dissipation rate equation we obtain

$$\left(\frac{Sk}{\varepsilon}\right)_\infty = \frac{1}{-2b_{12_\infty}} \frac{\left(C_{\varepsilon_2} - 1\right)}{\left(C_{\varepsilon_1} - 1\right)\left(1 - C_P\right)}. \tag{4.25}$$

Finally for GG-I the production to dissipation ratio can be written as

$$\left(\frac{P}{\varepsilon}\right)_\infty = \frac{C_{\varepsilon_2} - 1}{C_{\varepsilon_1} - 1 + C_P}, \tag{4.26}$$

and for GG-II

$$\left(\frac{P}{\varepsilon}\right)_\infty = \frac{C_{\varepsilon_2} - 1}{\left(C_{\varepsilon_1} - 1\right)\left(1 - C_P\right)}. \tag{4.27}$$

It is interesting to note that the asymptotic P/ε from both the traditional dissipation model equation (GG-I) and the spectral by-pass model equation (GG-II) exhibit dependence on the production-blockage term C_P. In the GG-I model this is due to the direct effect of energy transfer from dilatational kinetic to internal form. This represents the physics that not all of the energy extracted from the mean flow by production resides in the kinetic form. A portion proportional to C_P is converted to internal energy. The GG-II model additionally incorporates the indirect effect of the kinetic–internal energy exchange on the spectral cascade and hence dissipation.

Following the incompressible SSG (Speziale *et al.* 1991) dissipation rate evolution equation for both GG-I and GG-II we use

$$C_{\varepsilon_1} = 1.44, \quad C_{\varepsilon_2} = 1.83. \tag{4.28}$$

As mentioned in § 3.5, viscosity variation does not affect the dissipation evolution significantly. The fixed points of the anisotropy tensor can now be calculated using (4.26) or (4.27) in (4.19)–(4.22). As expected, the fixed points of homogeneous shear depend exclusively on the closure model coefficients of the dissipation rate equation and pressure–strain correlation closure. By requiring consistency between the model asymptotic behaviour depicted in (4.19)–(4.22) and DNS results, we can determine the model coefficients.

4.4. *Model closure using DNS*

The DNS of compressible homogeneous shear performed by Sarkar (1995) provides full time history evolution of the anisotropy tensor b_{ij}, normalized dilatation X_ε, and normalized growth rates of turbulent kinetic energy Λ, for four cases of different initial gradient Mach number. Each simulation, characterized by the initial gradient Mach number, leads to a different set of asymptotic values for the five quantities of interest. We use the long time behaviour of the five quantities b_{11}, b_{22}, b_{12}, X_ε and Λ to determine the five coefficients of the pressure–strain correlation C_1, C_3, C_4, C_5, and C_P based on the initial gradient Mach number of each DNS case. Sarkar's DNS spans the range $0.51 \leqslant M_{g_0} \leqslant 3.05$. The normalized quantities X_ε and Λ are defined as

$$X_\varepsilon = \frac{\overline{\rho}\varepsilon - \Pi}{\overline{\rho}P}, \quad \Lambda = \frac{1}{Sk}\frac{\mathrm{d}k}{\mathrm{d}t}. \tag{4.29}$$

The gradient Mach number in (3.12) differs slightly from that calculated by Sarkar due to a different length scale definition. Whereas Sarkar uses an integral length scale in the transverse shearing direction, we employ a large-eddy length scale similar to the one used by Simone *et al.* (1997). Nonetheless, as shown by Simone *et al.* (1997),

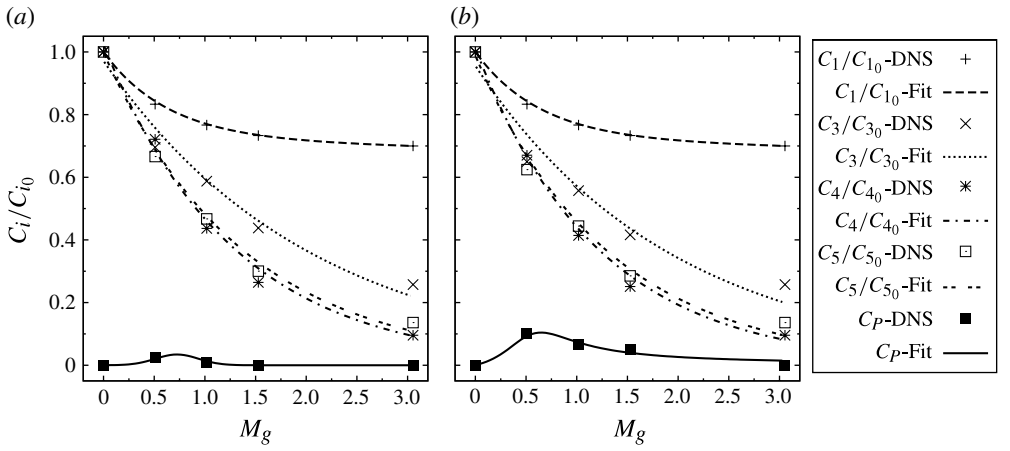

FIGURE 5. Calibrated coefficients for (*a*) GG-I, and (*b*) GG-II as functions of gradient Mach number. Symbols show best agreement with DNS (Sarkar 1995), lines are least-squares curve fits, given in appendix A by (A 1)–(A 4) and table 7.

C_{i_0}	SSG	SSG-S	LRR-IP	LRR	JM	GG-I	GG-II
C_{1_0}	3.4	3.4	3.6	3.0	3.0	3.0	3.0
$C^*_{1_0}$	1.8	1.8	—	—	—	—	—
C_{2_0}	4.2	4.2	—	—	—	—	—
C_{3_0}	0.8	0.8	0.8	0.8	0.82	0.82	0.82
$C^*_{3_0}$	1.3	1.3	—	—	—	—	—
C_{4_0}	1.25	1.25	1.2	1.75	1.59	1.59	1.59
C_{5_0}	0.4	0.4	1.2	1.31	1.09	1.12	1.12
C_{ε_1}	1.44	1.44	1.44	1.44	1.40	1.44	1.44
C_{ε_2}	1.83	1.90	1.90	1.90	1.90	1.83	1.83
α_1	—	0.5	—	—	—	—	—
α_2	—	0.15	—	—	—	—	—
α_3	—	0.2	—	—	—	—	—

TABLE 2. Pressure–strain correlation model coefficients.

both gradient Mach number definitions appropriately characterize compressibility effects.

The GG-I and GG-II pressure–strain correlation coefficients are calibrated with DNS at four non-zero gradient Mach numbers. To calibrate at the incompressible limit, i.e. $M_g = 0$, the equilibrium values found in the incompressible homogeneous shear experiments of Tavoularis & Corrsin (1981) are used. Figure 5 shows the dependence of the model coefficients on gradient Mach number, where C_{i_0} are the incompressible model coefficients. A comparison of the incompressible coefficients with existing models is shown in table 2. The least-squares curve fit functions and coefficients can be found in appendix A. The calibration of the GG-I and GG-II compressible pressure–strain correlation models is now complete. It is interesting to note that the production-blocking effect is significant only in the proximity of $M_g \approx 1$, which corresponds to Regime 2 of flow–pressure interactions. At higher M_g, the coefficients tend to very small values consistent with Regime 1 where the influence of pressure on

turbulence is negligible. Thus, our calibration methodology naturally yields physically consistent behaviour.

Calibration for a broader range of compressible homogeneous flows with different mean-flow gradients can be achieved in a similar fashion. Preliminary steps towards such a calibration applied to two-dimensional incompressible turbulence is outlined in Mishra & Girimaji (2010). Accordingly, the coefficients would also be functions of mean-flow-gradient invariants. Cambon *et al.* (1993) point out that compressibility effects may enhance turbulent kinetic energy for axial compression. Such behaviour can be easily accommodated through increased P/ε by sensitizing C_P to mean-flow-gradient invariants. Here we restrict ourselves to shear-dominated flows as reliable data of compressible homogeneous turbulence for other flows is currently unavailable.

4.5. *Preliminary model assessment*

The model development takes into account only the asymptotic state of Reynolds stress anisotropy. Such a model cannot guarantee correct transient behaviour or the prediction of other flow parameters in compressible homogeneous shear flow. Unlike the asymptotic behaviour, the transient behaviour is strongly dependent upon the initial wave-vector distribution and hence not unique. Nevertheless, we compare the model computations against DNS at the transient stages. The objective here is not a quantitative comparison, but to examine if the model captures the correct trends with increasing Mach numbers.

For this validation, we numerically integrate (4.8) and (4.10) using a fourth-order Runge–Kutta–Fehlberg numerical scheme. The initial conditions match those found in Sarkar's DNS: isotropic Reynolds stresses, gradient Mach number, turbulent Mach number, and Sk/ε. Figures 6 and 7 show the results obtained for GG-I and GG-II respectively. It is clear that both models are able to capture the essential physical features seen in compressible homogeneous shear DNS. Specifically both models display the following characteristics as the initial gradient Mach number increases:

(a) increase in Reynolds stress anisotropy, figures 6(a) and 7(a);

(b) reduction of shear Reynolds stress and therefore production, figures 6(b) and 7(b);

(c) reduction of normalized growth rates of turbulent kinetic energy, figures 6(c) and 7(c);

(d) long time behaviour of dilatational effects is insensitive to initial gradient Mach number, figures 6(d) and 7(d).

Using (4.26) and (4.27), the production to dissipation ratio at equilibrium for homogeneous shear is plotted in figure 8. The models display different behaviour at intermediate M_g due to the exclusion (GG-I) or inclusion (GG-II) of the C_P term in the dissipation rate equation (3.11). For the range shown in figure 8 the average production to dissipation ratios are 1.86 and 1.97 for the GG-I and GG-II models respectively. These average values are not significantly different from the LRR (Launder *et al.* 1975) or SSG (Speziale *et al.* 1991) equilibrium production to dissipation ratios for homogeneous shear, as seen in figure 8. Therefore the difference in P/ε ratio is not significant.

We now compare our pressure–dilatation model with the one derived by Sarkar (1992). By performing an order-of-magnitude analysis of the fluctuating pressure equation, Sarkar obtained the following pressure–dilatation model:

$$\Pi = 2\alpha_2 \overline{\rho} k M_t \frac{\partial \tilde{u}_m}{\partial x_n} b_{mn} + \alpha_3 \overline{\rho} \varepsilon M_t^2. \tag{4.30}$$

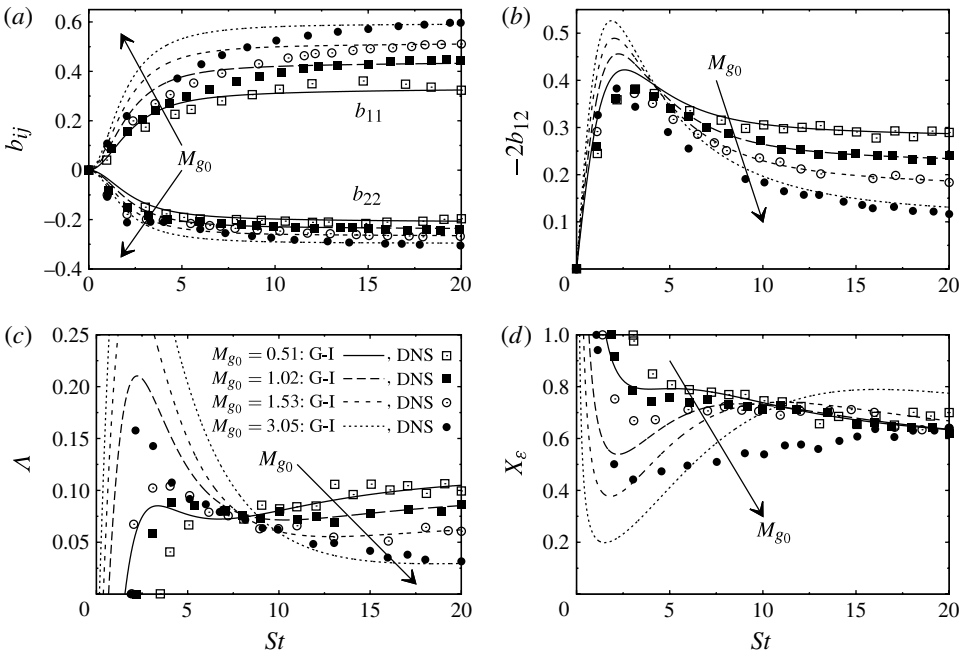

FIGURE 6. GG-I model preliminary validation with the compressible homogeneous shear DNS of Sarkar (1995); arrows point towards increasing initial gradient Mach number. (*a*) b_{11} and b_{22}, (*b*) b_{12}, (*c*) Λ, and (*d*) X_ε.

Some similarity between the present model, (3.8), and Sarkar model, (4.30), is clearly evident. However, the main difference lies in the trends as a function of Mach number. Whereas the Sarkar model suggests increasing energy transfer from kinetic to internal form as M_t increases, the present model shows maximum transfer when acoustic and shear time scales are of the same order. For the present closure model at excessively high Mach numbers, the transfer vanishes, consistent with no flow-thermodynamic interactions in Regime 1.

Overall the compressible pressure–strain correlation models GG-I and GG-II possess three notable features. First, for low gradient Mach number, i.e. the incompressible limit, the model coefficients are very close to those of the Jones & Musonge (1988) incompressible pressure–strain correlation model as seen in table 2. If desired, one may set $C_{3_0} = 0.8$ to satisfy the Crow (1968) constraint without a significant impact on model performance. Second, as DNS (Freund *et al.* 2000; Pantano & Sarkar 2002) has shown, for very large gradient Mach number the effect of the pressure–strain correlation is diminished, as can be observed in figures 5 and 9. And third, the inclusion of the production-blocking term suggested by RDT (Bertsch 2010) allows the GG-I and GG-II models to capture the long time behaviour of the normalized dilatational effects X_ε fairly well for the intermediate gradient Mach number calibrations, as seen in figures 6(*d*) and 7(*d*). The models display consistency with RDT behaviour at low, intermediate and high gradient Mach number. This attribute enables both GG-I and GG-II to capture a range of physics beyond the scope of calibration alone.

A final observation regarding figures 6 and 7 is in order to explain the lack of agreement between model and data at small *St*. There are two principal reasons. First,

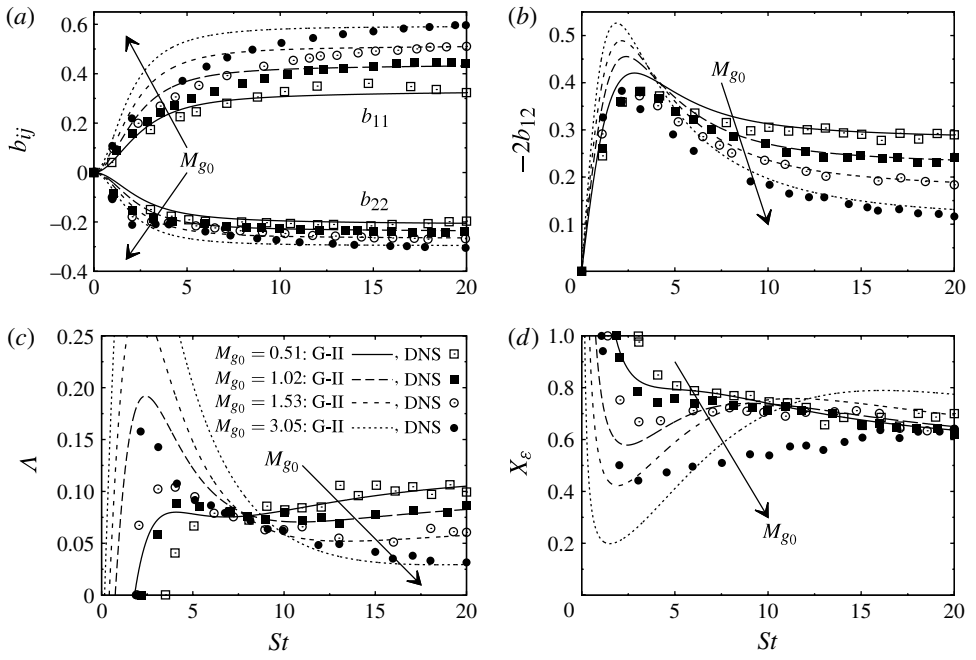

FIGURE 7. GG-II model preliminary validation with the compressible homogeneous shear DNS of Sarkar (1995); arrows point towards increasing initial gradient Mach number. (*a*) b_{11} and b_{22}, (*b*) b_{12}, (*c*) Λ, and (*d*) X_ε.

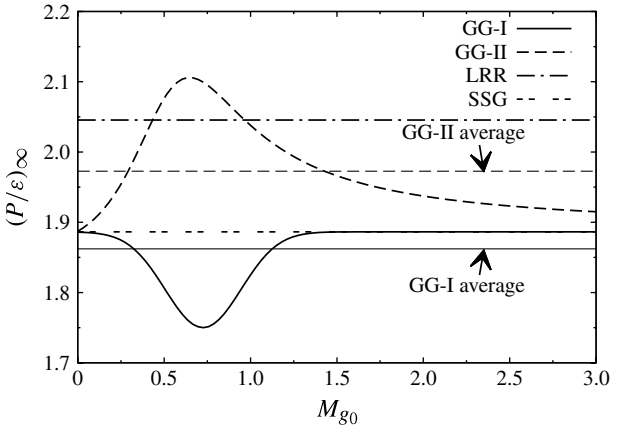

FIGURE 8. Production to dissipation ratios at equilibrium for homogeneous shear.

it is important to point out that a more accurate model representation of the interim behaviour can be obtained if the acoustic length scale is employed in the gradient Mach number definition. However, as mentioned earlier, this length scale requires a separate closure model. The second reason is more critical. The main challenge of any pressure–strain correlation model is to determine the closure expression without any knowledge of the wavenumber content of the flow and thermodynamic fields.

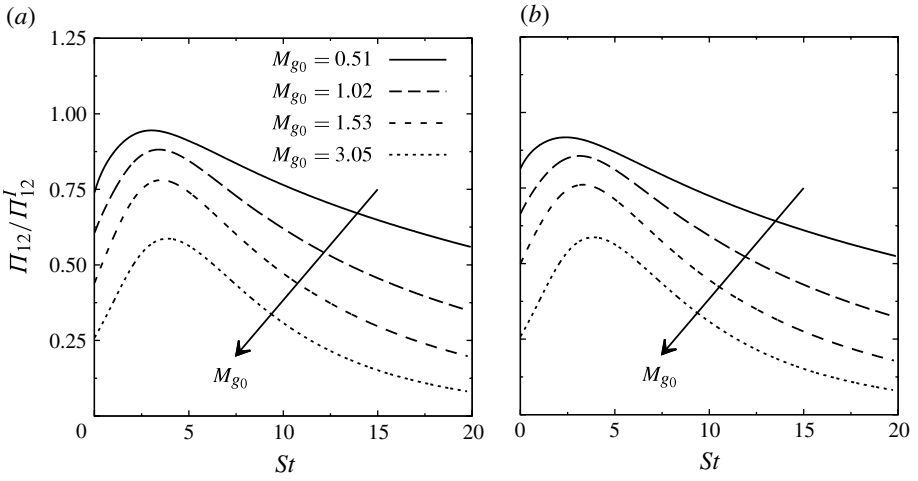

FIGURE 9. Evolution of compressible to incompressible pressure–strain correlation ratio for different initial gradient Mach numbers, (*a*) GG-I, (*b*) GG-II.

Thus, by definition, pressure–strain correlation modelling in terms of only second moments is an ill-posed problem. For example, two DNS calculations with the same Reynolds stress initial condition, but with different wavenumber content can evolve quite differently. However, given the limitations of single-point closure, both flows will elicit the same closure model. Therefore, the models are derived based on a 'seasoned' or 'aged' wave-vector field. Any arbitrary initial condition will soon pass through transient stages and reach the seasoned state. Finally it approaches the asymptotic state via the seasoned state. As pointed out by Simone *et al.* (1997), the initial conditions used in Sarkar's DNS were not properly aged to become representative of a 'physical' turbulent field. Thus, no single-point closure model, lacking wave-vector information, can be expected to capture the transient behaviour precisely. Furthermore, the behaviour of GG-I and GG-II for small St shown in figures 6(*b*), 7(*b*), 6(*c*), and 7(*c*) agrees very well qualitatively with the DNS of Simone *et al.* (1997) that employs more physically consistent initial conditions.

5. Model validation: high-speed mixing layer

One of the biggest challenges in the development of a compressible pressure–strain correlation is the ability to capture the reduction of normalized supersonic mixing-layer growth rates observed experimentally by Papamoschou & Roshko (1988), Goebel & Dutton (1991), Clemens & Mungal (1995), and many others (Kline *et al.* 1982; Chinzei *et al.* 1986; Samimy & Elliot 1990; Hall, Dimotakis & Rosemann 1993). In this section we present the results of incorporating compressible pressure–strain correlations GG-I and GG-II into the ANSYS® FLUENT Reynolds stress solver. To compare with existing popular models, we perform calculations with the incompressible LRR (Launder *et al.* 1975), and compressible SSG-S (Speziale *et al.* 1991; Sarkar 1992) models. We match the boundary conditions encountered in the experiments of Goebel & Dutton (1991) as closely as possible to compare similarity profiles, mixing-layer spreading rates and Reynolds stresses. Details are provided in appendix B.

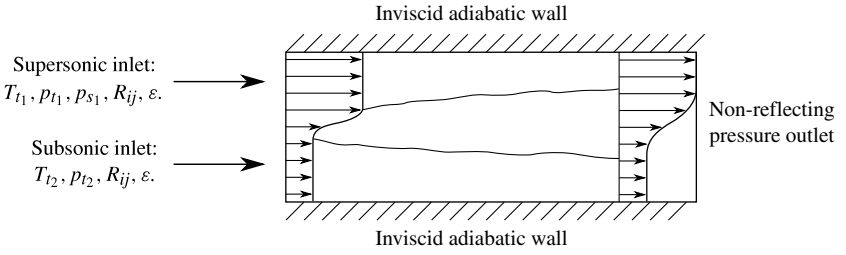

FIGURE 10. Two-dimensional supersonic mixing-layer boundary conditions.

Case	M_r	M_1	M_2	U_1 (m s^{-1})	U_2 (m s^{-1})	T_{t_1} (K)	T_{t_2} (K)	p_{t_1} (kPa)	p_{t_2} (kPa)	p_{s_1} (kPa)
C1	0.40	2.01	1.38	515	404	295	295	365.6	142.3	46
C2	0.91	1.91	1.36	700	399	578	295	333.4	147.4	49
C3	1.37	1.96	0.27	499	92	285	285	389.7	55.8	53
C4	1.73	2.35	0.30	616	100	360	290	486.8	38.3	36
C5	1.97	2.27	0.38	830	131	675	300	381.8	35.4	32

TABLE 3. Supersonic mixing-layer inlet conditions.

Three grids are studied to ensure grid insensitivity. The coarse grid consists of 24 000 cells (300 by 80), the medium grid 48 000 cells (400 by 120), and the fine grid 96 000 cells (600 by 160). It is concluded that the medium grid provides adequate resolution due to the negligible difference between the medium and fine grid results.

The experimental setup of a two-dimensional mixing layer consists of a channel with two incoming streams separated by a splitter plate. The top stream is labelled as 'primary' and the lower as 'secondary'. It is customary to choose the primary stream as the high-speed inlet. For the computations we use a rectangular domain downstream of the splitter plate to avoid any near-wall effects. A schematic of the computational domain along with the type of boundary conditions is shown in figure 10. The domain is 0.3 m long in the streamwise direction and 0.1 m high in the cross-stream direction. At the inlet, the Reynolds stress tensor is isotropic. We use hyperbolic-tangent and piecewise-cubic polynomial functions to set the boundary conditions at the inlet to avoid sharp gradients and to expedite a fully developed self-similar flow. The flow becomes self-similar between 0.1 and 0.2 m downstream of the inlet for all cases. Table 3 summarizes the inlet conditions where the subscripts s and t refer to static and total quantities respectively.

Goebel & Dutton (1991) characterize the mixing layer using a relative Mach number defined as

$$M_r \equiv \frac{U_1 - U_2}{(a_1 + a_2)/2} = \frac{\Delta U}{\bar{a}}, \tag{5.1}$$

where the subscripts 1 and 2 refer to the primary and secondary streams respectively, U is the mean inlet velocity, and $\bar{a}$ is the average inlet speed of sound. Papamoschou & Roshko (1988) observed that overall compressibility effects are found mainly

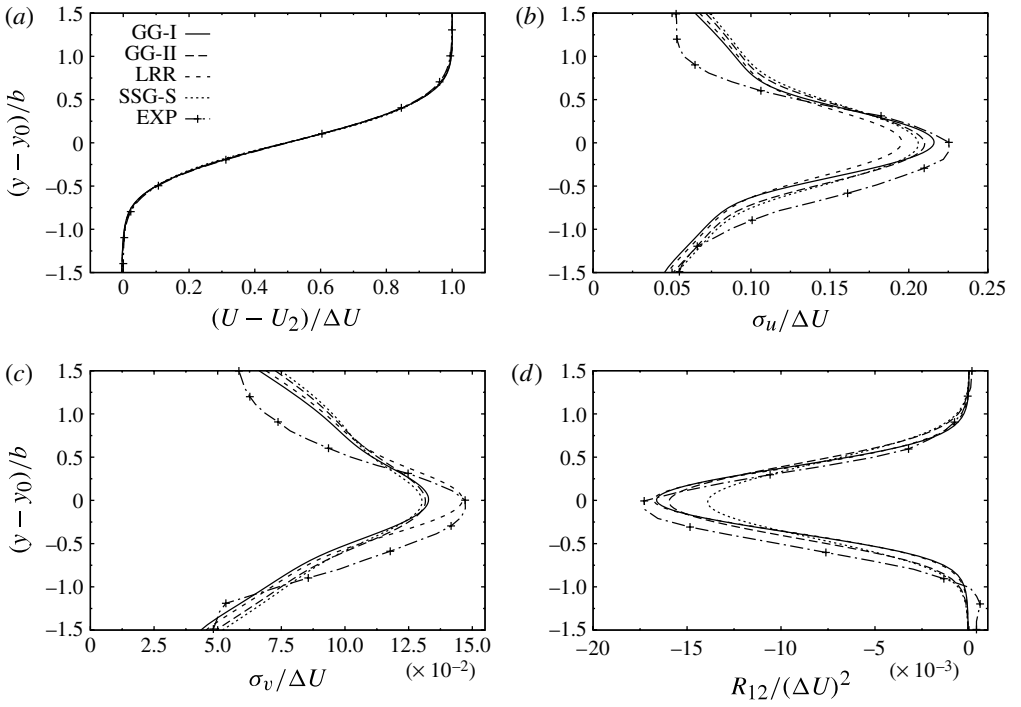

FIGURE 11. SMC mixing-layer results for C1, $M_r = 0.40$: (*a*) streamwise velocity similarity profile; (*b*) normalized streamwise Reynolds stress; (*c*) normalized cross-stream Reynolds stress; (*d*) normalized shear Reynolds stress.

between $0.5 \leqslant M_r \leqslant 2.0$. Goebel & Dutton's experiments span this range of M_r going from 0.4 to 1.97. Here we present results for five of their cases: $M_r = 0.40, 0.91,$ 1.37, 1.73, and 1.97, which in table 3 and the following are referred to as C1, C2, C3, C4, and C5 respectively.

Figures 11–15 compare similarity profiles $(U - U_2)/\Delta U$; normalized streamwise Reynolds stresses $\sigma_u/\Delta U$; normalized cross-stream Reynolds stresses $\sigma_v/\Delta U$; and normalized shear Reynolds stresses $R_{12}/(\Delta U)^2$ of SMC results against experimental data for each of the five cases. All results are plotted in the self-similar region of the flow. In these plots b is the mixing-layer thickness defined as the transverse distance between locations where the mean streamwise velocity is $U_1 - 0.1\Delta U$ and $U_2 + 0.1\Delta U$. The y coordinate of the mixing-layer centreline is y_0. The standard deviations of the Reynolds stresses are defined as

$$\sigma_u = \sqrt{R_{11}}, \quad \sigma_v = \sqrt{R_{22}}. \tag{5.2}$$

5.1. *Similarity profiles*

Figures 11(*a*), 12(*a*), 13(*a*), 14(*a*), and 15(*a*) compare the similarity profiles obtained from each model against experimental data for the different Mach number cases. Although not shown here, multiple cross-sections were plotted to ensure that the flows are fully self-similar. The experimental similarity profile is taken to be the error-function curve fit that Goebel & Dutton found to be universal in all their cases.

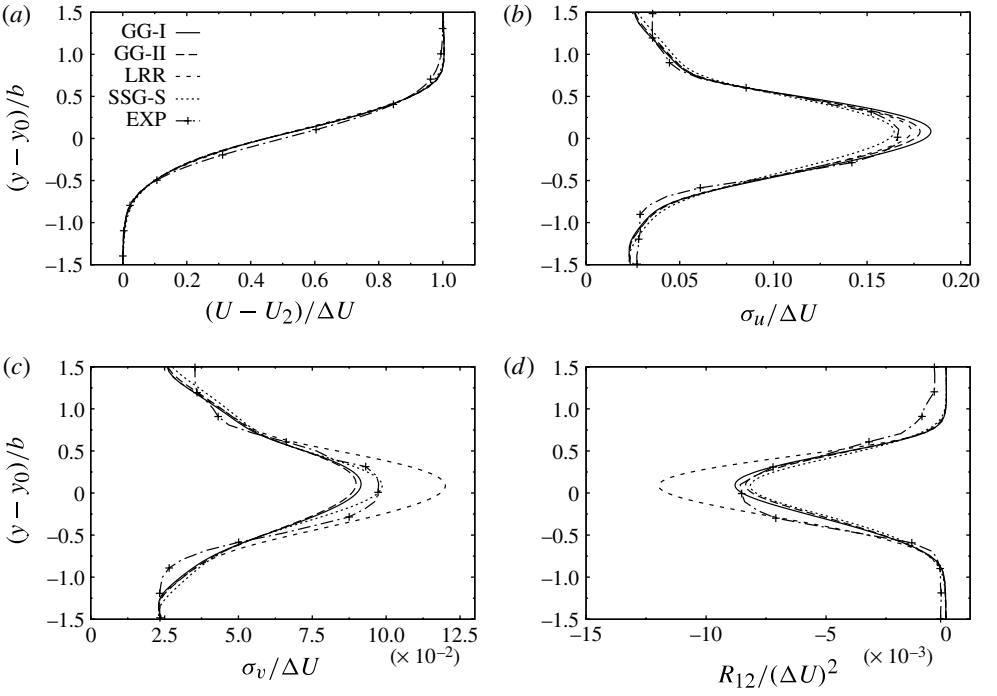

FIGURE 12. SMC mixing-layer results for C2, $M_r = 0.91$: (*a*) streamwise velocity similarity profile; (*b*) normalized streamwise Reynolds stress; (*c*) normalized cross-stream Reynolds stress; (*d*) normalized shear Reynolds stress.

All models capture the self-similar profile for the five mixing-layer cases reasonably well.

5.2. *Streamwise Reynolds stresses*

Figures 11(*b*), 12(*b*), 13(*b*), 14(*b*), and 15(*b*) compare the normalized streamwise Reynolds stresses. For the lowest two relative Mach number cases, all models perform fairly well in matching the experimental data as seen in figures 11(*b*) and 12(*b*). However as the relative Mach number increases, the present models GG-I and GG-II show improvement in capturing the peak value of normalized streamwise Reynolds stress compared to the LRR and SSG-S models, as seen in figures 13(*b*)–15(*b*).

5.3. *Cross-stream Reynolds stresses*

Figures 11(*c*), 12(*c*), 13(*c*), 14(*c*), 15(*c*) compare the normalized cross-stream Reynolds stresses. These figures show that the GG-I and GG-II models do a significantly better job of capturing the reduction of the cross-stream Reynolds stresses as the relative Mach number is increased. Figure 17(*b*) below compares the Reynolds stress anisotropy σ_u/σ_v computed for each model at different relative Mach numbers. Since an isotropic Reynolds stress tensor is used at the inlet for all simulations, the anisotropy found in the fully developed region is almost entirely due to the effect of the pressure–strain correlation. From figure 17(*b*) it is clear that whereas the GG-I and GG-II models are able to capture the trend of increasing anisotropy with increasing relative Mach number, both the LRR and SSG-S models predict almost constant values of anisotropy regardless of the relative Mach number of the mixing layer.

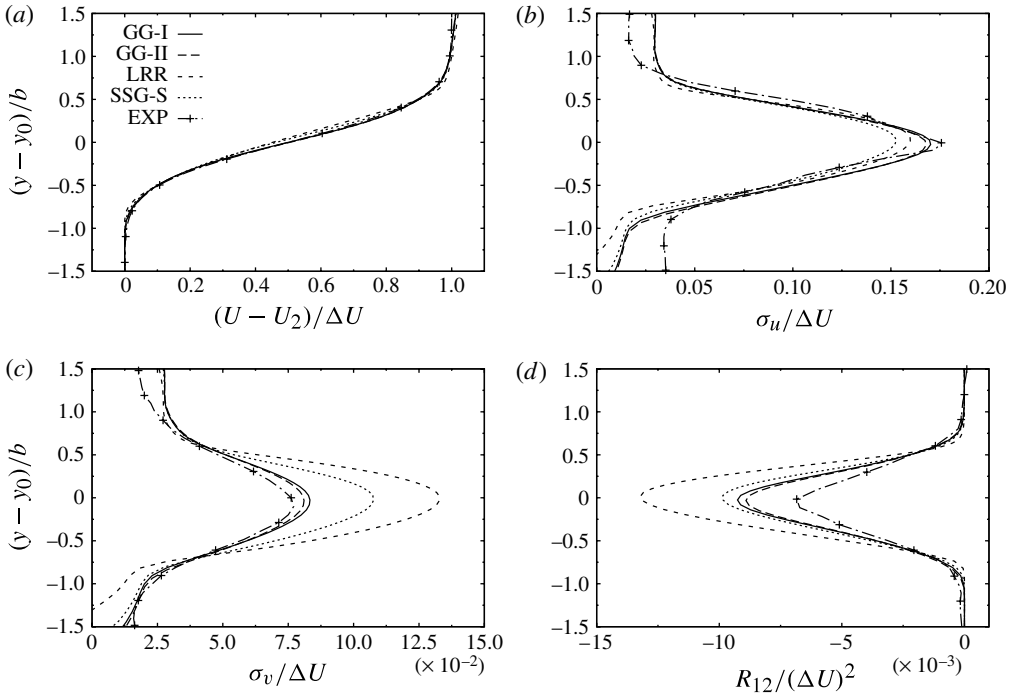

FIGURE 13. SMC mixing-layer results for C3, $M_r = 1.37$: (*a*) streamwise velocity similarity profile; (*b*) normalized streamwise Reynolds stress; (*c*) normalized cross-stream Reynolds stress; (*d*) normalized shear Reynolds stress .

5.4. *Shear Reynolds stresses*

Figures 11(*d*), 12(*d*), 13(*d*), 14(*d*), and 15(*d*) compare the normalized shear Reynolds stress. It is clear that the GG-I, GG-II, and SSG-S models predict the reduction of the shear Reynolds stress as the relative Mach number increases fairly well, whereas the LRR model lacking compressibility corrections does not. Being able to predict both the reduction of shear Reynolds stress as well as the increase in Reynolds stress anisotropy σ_u/σ_v is of paramount importance to capture the reduced spreading rates for compressible mixing-layers. Capturing only one of the two trends indicates that the physics is not well represented by the model. It may be useful to recall that in Regime 2, the Reynolds shear stress level diminishes due to pressure effects blocking production. This physics is incorporated into the present closure model.

5.5. *Spreading rates*

Figure 16 shows a compilation of experimental data (Kline *et al.* 1982; Chinzei *et al.* 1986; Papamoschou & Roshko 1988; Samimy & Elliot 1990; Goebel & Dutton 1991; Hall *et al.* 1993; Clemens & Mungal 1995) for normalized mixing-layer spreading rates as a function of relative Mach number. We can immediately observe that there is a significant disparity among the experimental data. The Langley curve appears to mark an upper limit, while the experiments of Hall *et al.* (1993) represent the lower limit. The experiments of Goebel & Dutton (1991) fall in the middle of these two limits making their results a good data set for model validation. Figure 17(*a*) shows

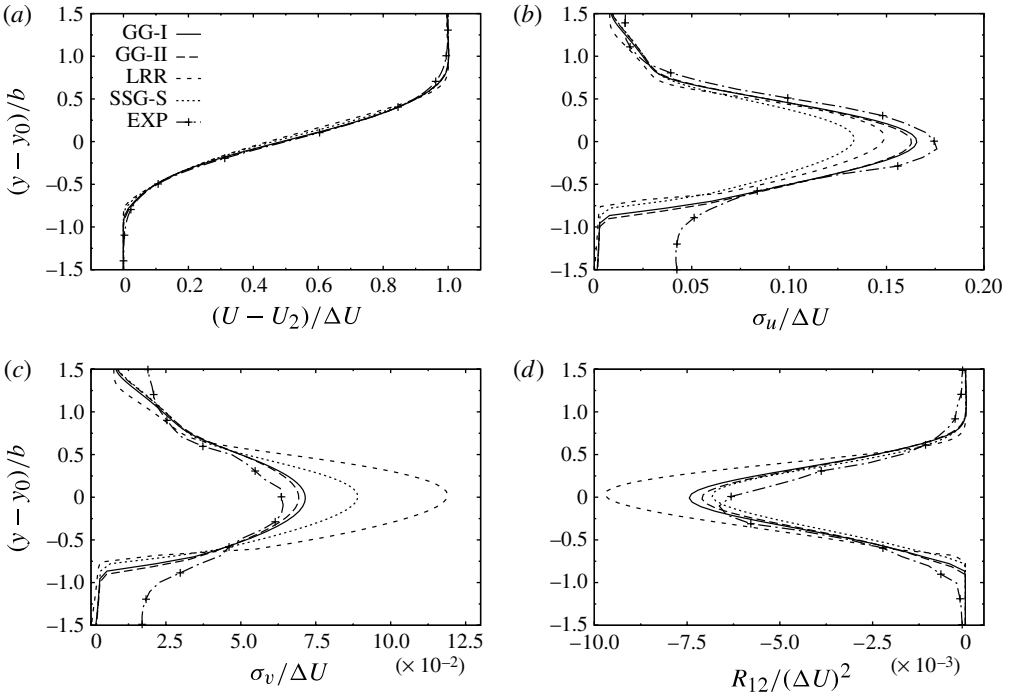

FIGURE 14. SMC mixing-layer results for C4, $M_r = 1.73$: (*a*) streamwise velocity similarity profile; (*b*) normalized streamwise Reynolds stress; (*c*) normalized cross-stream Reynolds stress; (*d*) normalized shear Reynolds stress.

the normalized spreading rates of the SMC calculations, where the incompressible spreading rates are estimated as (Papamoschou & Roshko 1988; Goebel & Dutton 1991)

$$\left(\frac{\mathrm{d}b}{\mathrm{d}x}\right)_i = 0.0825\frac{(1-r)\left(1+s^{1/2}\right)}{1+rs^{1/2}}, \quad r = \frac{U_2}{U_1}, \quad s = \frac{\rho_2}{\rho_1}. \tag{5.3}$$

The LRR model does not include any compressibility corrections and therefore overpredicts the spreading rates for all five cases, although it does capture to a small degree the overall trend of reduced normalized spreading rates as the relative Mach number increases. The SSG-S model, which is specifically calibrated for compressible shear layers, does a reasonable job of approximating the experimental values, albeit by using a compressible dissipation model (Sarkar *et al.* 1991*a*). On the other hand, the GG-I and GG-II models do an excellent job of predicting the normalized spreading rates, while more closely capturing the experimental anisotropy of the Reynolds stresses. Table 4 shows the mixing-layer spreading rates for each model as well as the experimental values. The incompressible LRR model, as expected, overpredicts the spreading rates, and the SSG-S model provides a reasonable first approximation, averaging about a 20 % error. The present compressible pressure–strain correlation models GG-I and GG-II are generally less than 10 % in error with respect to the experimental spreading rates.

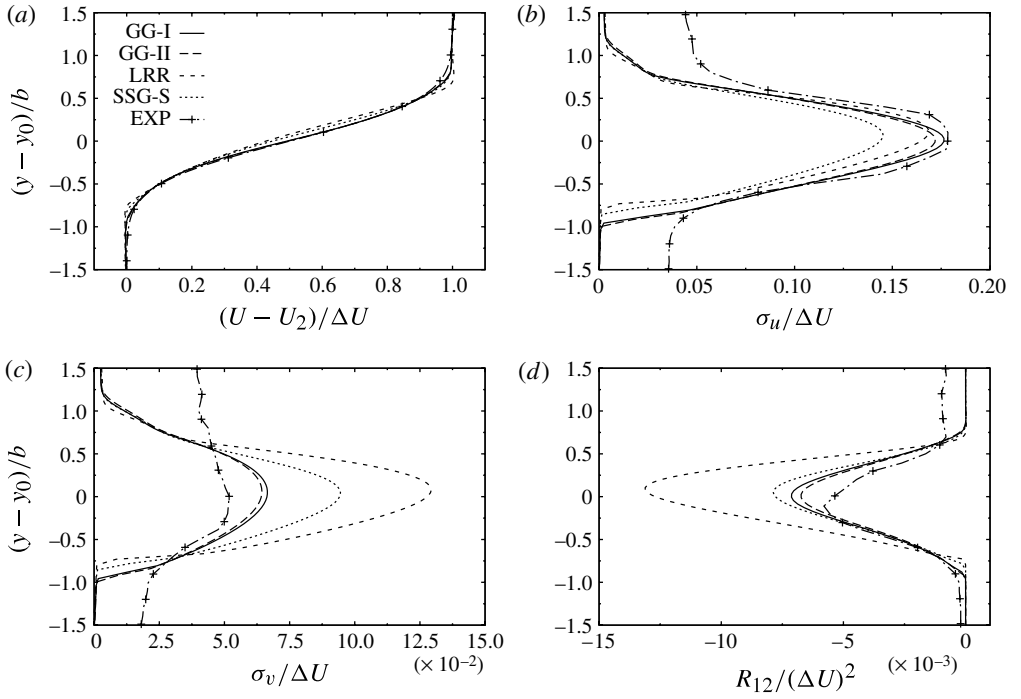

FIGURE 15. SMC mixing-layer results for C5, $M_r = 1.97$: (*a*) streamwise velocity similarity profile; (*b*) normalized streamwise Reynolds stress; (*c*) normalized cross-stream Reynolds stress; (*d*) normalized shear Reynolds stress.

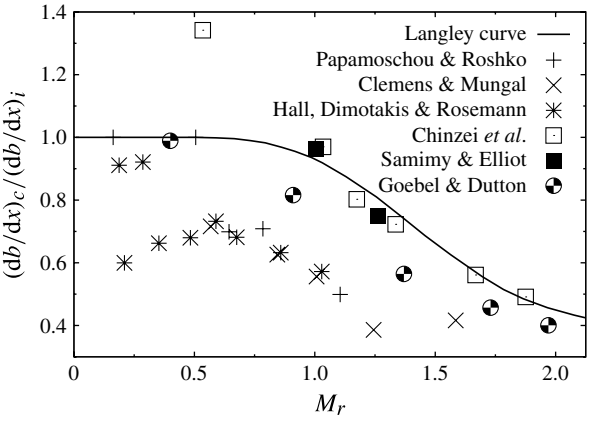

FIGURE 16. Normalized experimental spreading rates.

5.6. *GG-I and GG-II model coefficient behaviour*

Figure 18 shows the variation of the normalized pressure–strain correlation coefficients inside the mixing layer for both the quasi-incompressible case C1 and highly compressible case C5. Whereas the lower relative Mach number case displays only a minor deviation from incompressible behaviour, case C5 shows how compressibility

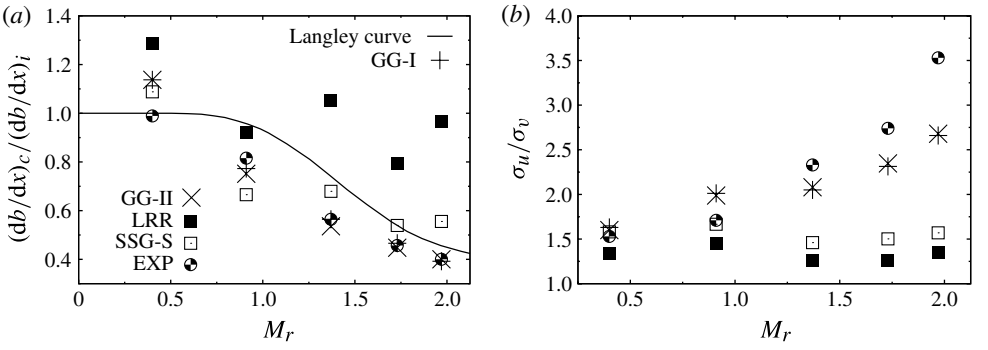

FIGURE 17. SMC mixing-layer results: (*a*) normalized spreading rates, where db/dx_i comes from (5.3); (*b*) Reynolds stress anisotropy.

Case	LRR	SSG-S	GG-I	GG-II	Experimental
C1	0.026	0.022	0.023	0.023	0.020
C2	0.043	0.031	0.036	0.035	0.038
C3	0.110	0.071	0.059	0.056	0.059
C4	0.087	0.059	0.051	0.049	0.050
C5	0.118	0.068	0.048	0.049	0.049

TABLE 4. Mixing-layer spreading rates, db/dx.

effects become dominant at higher relative Mach number. Figure 18 provides additional support for the selection of gradient Mach number as an appropriate parameter for characterizing compressibility effects.

5.7. *Comparison against two-equation models*

The final step of the mixing-layer study is a comparison of the present SMC model against representative two-equations models: standard k–ε, and k–ε–S that include the so-called Sarkar correction (Sarkar *et al.* 1991*a*), and the explicit algebraic Reynolds stress model (EARSM) of Girimaji (1996). The mixing-layer growth rate and anisotropy profiles are shown in figures 19(*a*) and 19(*b*) respectively. The growth rates at different Mach numbers are normalized by growth rates of incompressible mixing layers at the same velocity and density ratio, see (5.3). The results can be summarized as follows.

(*a*) The standard k–ε model, which is well tuned for the incompressible mixing layer, performs very well in predicting the mixing-layer thickness at the lowest Mach number considered. However at higher Mach numbers the model does not produce the requisite degree of growth rate reduction. The model completely fails in capturing the increase in turbulence anisotropy at high Mach number. This is clearly a failure of the standard Boussinessq approximation.

(*b*) The EARSM does not include any compressibility correction yet performs marginally better than the standard k–ε model in predicting the mixing suppression. The improved nonlinear constitutive relation enables this model to capture

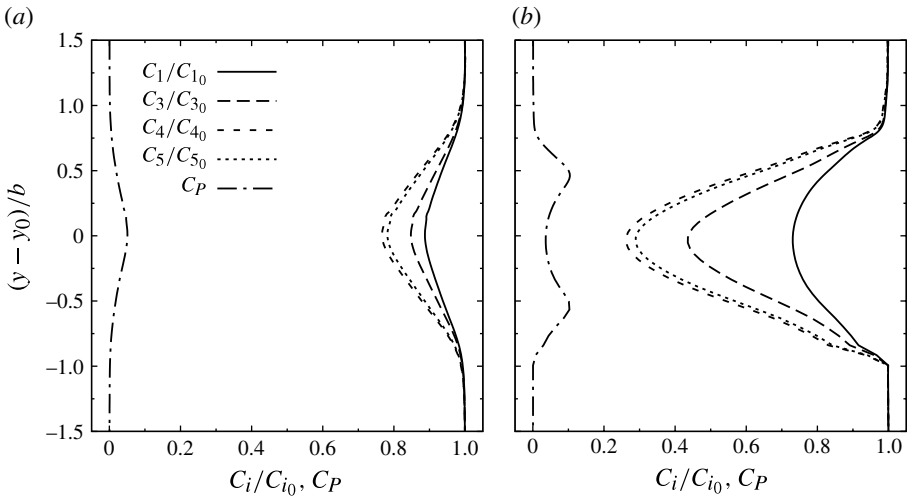

FIGURE 18. Normalized GG-II model coefficients for (*a*) C1, and (*b*) C5.

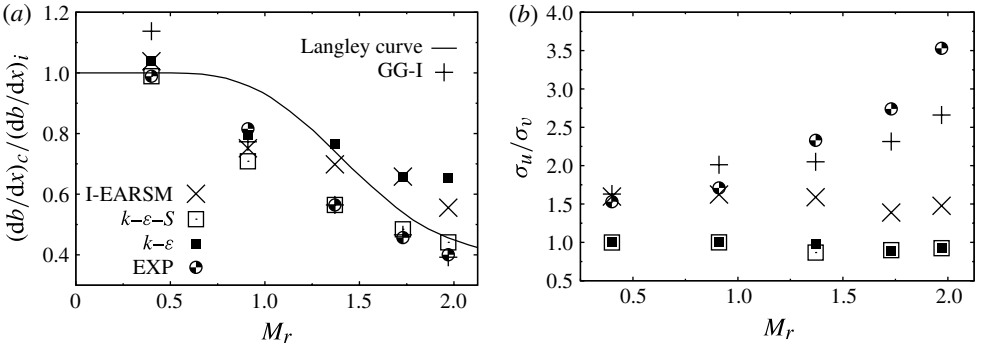

FIGURE 19. Comparison of SMC mixing-layer results with two-equation models: (*a*) normalized spreading rates, where $\mathrm{d}b/\mathrm{d}x_i$ comes from (5.3); (*b*) Reynolds stress anisotropy.

the anisotropy reasonably well at low Mach numbers. However, lacking any compressibility correction to the constitutive relation, the model does not reproduce the increasing anisotropy at high Mach numbers.

(*c*) The k–ε–S model with the Sarkar compressibility correction (Sarkar *et al.* 1991*a*) produces the requisite reduction in mixing-layer growth rate at high Mach numbers. Indeed, this model was tuned to yield the correct growth rate. The limitation of the model is seen in the anisotropy calculations in figure 19(*b*). Clearly, the calculated anisotropy is nearly independent of Mach number in direct contrast to experiments.

(*d*) As seen before, the present SMC model (GG-I) produces the appropriate variations in mixing-layer thickness and anisotropy with increasing Mach number. It should be reiterated here that the coefficients of GG-I were not calibrated specifically for mixing layers and yet capture the physics adequately well.

Set	γ^*	β	σ_ω	σ_d
1	0.518	0.0747	0.53 (1.0)	1.0
2	0.44	0.0828	1.0	0.4

TABLE 5. Model coefficients used in the Hellsten (2005) ω equation. Modified values are noted between parenthesis.

6. Boundary-layer study

High-speed boundary layers pose additional modelling challenges pertaining to near-wall phenomena not encountered in mixing-layers and other free shear flows. For example, the thermal boundary condition at the wall – adiabatic versus constant temperature, cold versus heated – can have a major influence on the velocity field. The closure model for turbulent heat flux (or equivalently turbulent Prandtl number) plays a critical role, see Bowersox (2009). Furthermore, low-Reynolds-number and wall-reflection physics which are important in subsonic boundary layers may also play a vital role. All these closures introduce further model coefficients. Accurate calibration of those terms goes outside the scope of this work. Here established low-speed models are used for those effects. Thus the purpose of the present computations is not to achieve perfect comparison with data, but to demonstrate that the novel pressure closures developed in this work lead to reasonable results.

6.1. *Numerical implementation*

Model computations are performed of a hypersonic boundary layer with free-stream Mach number of 7.2, and compared with the experimental data of Owen & Horstman (1972). Computations are also performed of a supersonic boundary layer with free-stream Mach number of 3.0; comparisons for this case are made with the DNS data of Duan, Beekman & Martín (2011). All models are tested using a standard turbulent heat-flux model, constant turbulent Prandtl number and no wall-reflection terms. For these computations the well-established EDGE code (http://www.foi.se/edge/) is used, which has been extensively validated in both internal and external flows (Eliasson 2005; Eliasson & Peng 2008). For better near-wall characteristics, the ω rather than the ε equation is used. The ω equation developed by Hellsten (2005) is employed:

$$\frac{\partial}{\partial t}(\overline{\rho}\omega) + \frac{\partial}{\partial x_i}(\overline{\rho}\omega\tilde{u}_i) = \frac{\partial}{\partial x_j}\left[(\mu + \mu_t\sigma_\omega)\frac{\partial \omega}{\partial x_j}\right] + \overline{\rho}\gamma^*\frac{\omega}{k}P - \overline{\rho}\beta\omega^2 + \frac{\overline{\rho}\sigma_d}{\omega}\max\left(\frac{\partial k}{\partial x_j}\frac{\partial \omega}{\partial x_j}; 0\right). \tag{6.1}$$

Dissipation is found by using

$$\varepsilon = \beta^* k\omega, \quad \beta^* = 0.09. \tag{6.2}$$

The constants γ^*, β, σ_ω, and σ_d vary according to

$$x = f_{mix}x_1 + (1 - f_{mix})\,x_2, \tag{6.3}$$

where the mixing function f_{mix} is similar to that of Menter (1994); for details see Hellsten (2005). The model coefficients are provided in table 5.

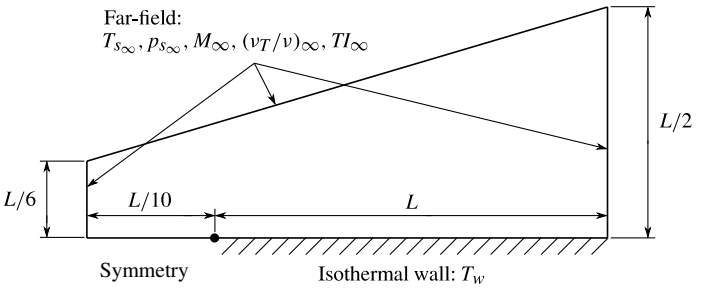

FIGURE 20. Two-dimensional supersonic boundary-layer boundary conditions.

Case	T_{s_∞} (K)	p_{s_∞} (kPa)	M_∞	$(\nu_T/\nu)_\infty$	TI_∞ (%)	T_w (K)	L (m)	Re_x (m^{-1})
M3	219.9	5.743	3.0	0.1	0.1	552	3.0	5.58×10^6
M7	58.67	0.681	7.2	0.1	0.1	310	3.0	11.6×10^6

TABLE 6. Supersonic boundary layer boundary conditions.

6.2. *Boundary conditions*

The boundary conditions are shown schematically in figure 20. Table 6 shows the values for each boundary condition as well as the Reynolds number per unit length defined as

$$Re_x = \frac{\overline{\rho}_\infty U_\infty}{\mu_\infty}. \tag{6.4}$$

The free-stream turbulence intensity is defined as $TI_\infty = \sqrt{2k_\infty/3}/U_\infty$. For the M7 case, the boundary conditions match the experiments of Owen & Horstman (1972), whereas for the M3 case they match the DNS data of Duan *et al.* (2011).

6.3. *Grid independence study*

Three grids are used to ensure grid independence. The coarse grid consists of 14 700 cells (105 by 140), the medium grid 30 000 cells (150 by 200), and the fine grid 58 800 cells (210 by 280). The agreement between medium and fine grids is excellent indicating grid independence.

6.4. *Objective of the study*

The objective of this study is to show that with simple near-wall modifications, the pressure-related closures can achieve acceptable agreement with experimental data. A comprehensive recalibration of the various ω-equation coefficients, which may depend on Mach number, is beyond the scope of this work. Towards the present objective, the following near-wall modifications are employed.

(*a*) The ω-equation coefficients can have a dramatic effect on the near-wall behaviour. The σ_ω closure coefficient controls the turbulent transport of specific dissipation rate. In standard models, this coefficient is typically varied between 0.5 and 1.0 (Wilcox 1988; Menter 1994; Hellsten 2005). To test the effect of modifying this term, computations are performed with both the blending function given by

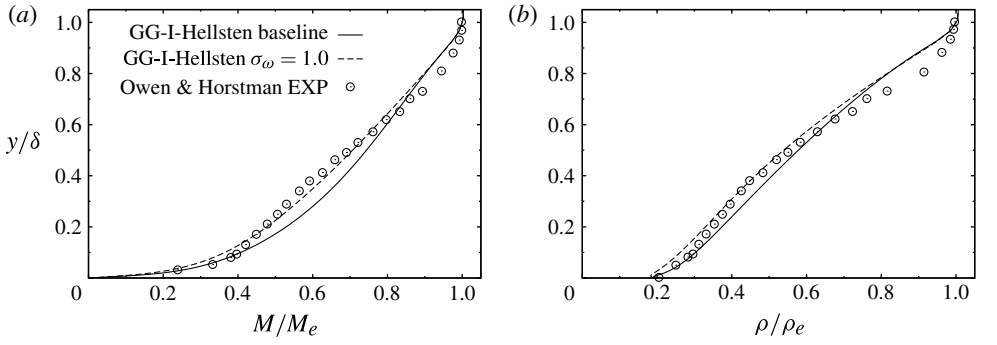

FIGURE 21. Flat-plate boundary layer, $M_\infty = 7.2$, effect of modifying σ_ω: (*a*) normalized Mach number; (*b*) normalized density.

Hellsten (2005), as well as a constant value of $\sigma_\omega = 1.0$. The values used in the Hellsten ω equation are provided in table 5.

(*b*) The length scale in the gradient Mach number definition may need to be adjusted for flow regions inside a boundary layer. Standard arguments for near-wall behaviour (Schlichting & Gersten 2000) lead to the length scaling as $l \sim d$, where d is the wall distance. In this study, the following three length scales are tested:

$$l = \frac{k^{3/2}}{\varepsilon} = \frac{k^{1/2}}{\beta^* \omega}, \tag{6.5a}$$

$$l = d, \tag{6.5b}$$

$$l = \min\left(d, \frac{k^{1/2}}{\beta^* \omega}\right). \tag{6.5c}$$

6.5. *Results*

6.5.1. *Modification of* σ_ω

The first results presented highlight the effect of modifying the σ_ω coefficient. Figures 21 and 22 compare model computations with the experimental data of Owen & Horstman (1972). In these figures δ is the boundary-layer thickness, and the subscript e refers to a value at the edge of the boundary layer. As is customary for compressible boundary layers, the van Driest transformation is used to compute u^+ (for details see White 1991):

$$u^+ = \frac{1}{\overline{u}_\tau} \int_0^{\tilde{u}} \left(\frac{\overline{\rho}}{\rho_w}\right)^{1/2} \mathrm{d}\tilde{u}, \quad \overline{u}_\tau = \left(\frac{\tau_w}{\rho_w}\right)^{1/2}, \quad \tau_w = \mu_w \left.\frac{\partial \tilde{u}}{\partial y}\right|_{y=0}, \quad y^+ = \frac{y \overline{u}_\tau}{\nu_w}. \tag{6.6}$$

The friction velocity is given by $\overline{u}_\tau$, and quantities evaluated at the wall are denoted by subscript w. Data are compared at the streamwise location $x = 2.37$ m. Figures 21(*a*) and 22(*a*) show a significant improvement in mean quantities by modifying the σ_ω coefficient. On the other hand, figure 22(*b*) shows that in van Driest coordinates the modification of σ_ω has a negligible effect on the GG-I model. Nonetheless, it is quite clear that overall better results are obtained by modifying the σ_ω coefficient to a constant value of unity. In the following, only models using a constant σ_ω coefficient are considered.

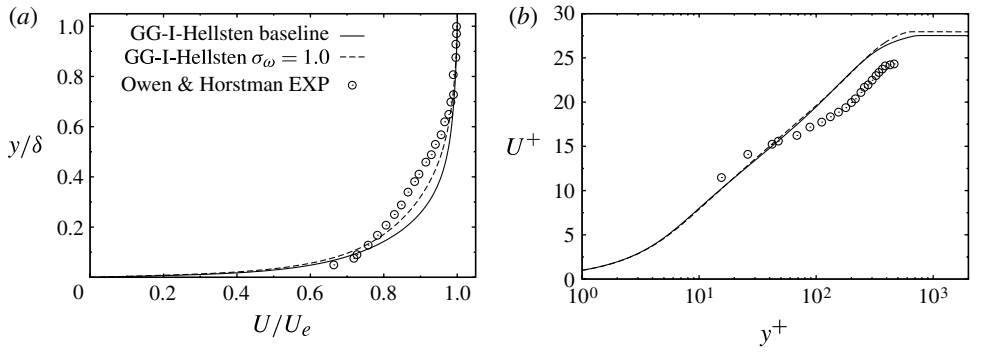

FIGURE 22. Flat-plate boundary layer, $M_\infty = 7.2$, effect of modifying σ_ω: (*a*) normalized streamwise velocity; (*b*) streamwise velocity in van Driest coordinates.

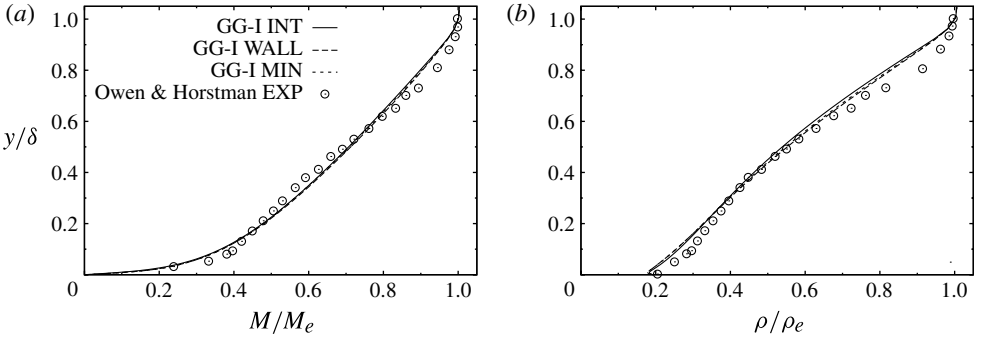

FIGURE 23. Flat-plate boundary layer, $M_\infty = 7.2$, effect of modifying l: (*a*) normalized Mach number; (*b*) normalized density.

6.5.2. *Near-wall length scale modification*

Figures 23 and 24 compare GG-I model computations using the three proposed length scale definitions with the data of Owen & Horstman (1972). The GG-I INT, GG-I WALL, and GG-I MIN models use the length scales defined in (6.5*a*), (6.5*b*) and (6.5*c*) respectively. From these figures it is evident that a modification to the length scale is required for the GG-I model to achieve satisfactory log-law behaviour. It can be seen that the GG-I MIN model achieves the best performance in van Driest coordinates. Therefore (6.5*c*) is chosen to be an adequate length scale for near-wall flow regions.

6.5.3. *Mach 3 comparison with DNS*

The GG-I MIN model computations are compared with the DNS data of Duan *et al.* (2011). Boundary layers with free-stream Mach number less than 5 typically exhibit negligible compressibility effects (Smits & Dussauge 2006). Thus, for these computations it is expected that the model will perform satisfactorily. Figure 25(*a*) compares normalized mean temperature profiles. The DNS data for mean temperature is taken to be the Crocco relation (Walz 1969), which Duan *et al.* (2011) found to be in excellent agreement with their simulations up to a free-stream Mach number of 12.0. It can be seen that the GG-I MIN model closely follows the DNS data of normalized mean temperature profile. Figure 25(*b*) shows the normalized streamwise

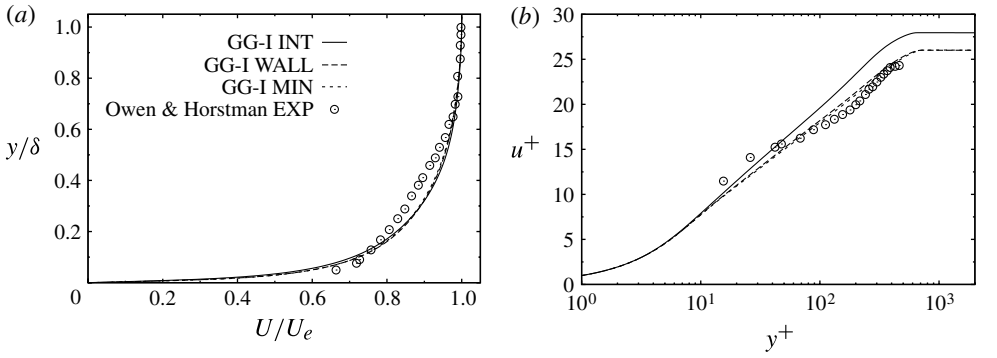

FIGURE 24. Flat-plate boundary layer, $M_\infty = 7.2$, effect of modifying l: (*a*) normalized streamwise velocity; (*b*) streamwise velocity in van Driest coordinates.

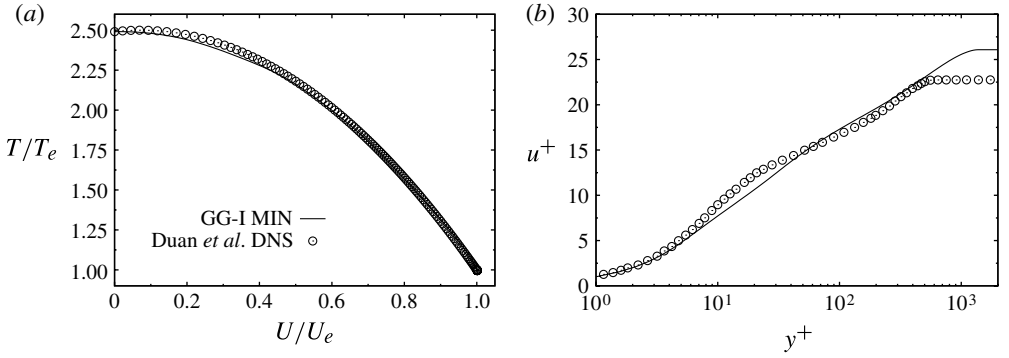

FIGURE 25. Flat-plate boundary layer, $M_\infty = 3.0$: (*a*) normalized mean temperature; (*b*) streamwise velocity in van Driest coords.

velocity profiles in van Driest coordinates. It is clear that the behaviour of the DNS data is reproduced fairly well, especially in the log-law region.

6.6. *Boundary-layer study findings*

In this section it is shown that by using simple near-wall corrections, the present compressible pressure–strain correlation model agrees well with both experimental (Owen & Horstman 1972) and direct numerical simulation (Duan *et al.* 2011) data of supersonic boundary layers. Two simple near-wall corrections are proposed: the first is to modify one of the parameters in the ω equation, and the second is to redefine the length scale in the gradient Mach number definition to be more consistent with traditional boundary-layer theory. The present results show that with these two simple modifications, the proposed pressure–strain correlation model can achieve adequate agreement with super- and hypersonic boundary layers.

7. Conclusions

Flow stabilization, increased anisotropy, flow–thermodynamics and spectral cascade modification are some of the critical effects of compressibility on turbulence in high-

speed flows. In this work, we commence with the development of a second-moment closure modelling framework in which all of the above effects can be accounted for in a self-consistent manner. Progress in second-moment closures is of intrinsic utility, and central to advancements in low-order RANS and high-fidelity variable-resolution computational methods for turbulence. Working towards physics-based second-moment closures we present closures for pressure–strain correlation, pressure–dilatation and the consequent effects on the spectral cascade/length scale equation. The physical foundation of the rapid pressure models is derived from RDT analysis which reveals a three-regime turbulence behaviour that depends on gradient Mach number. The functional form of the closure model is taken to be a pragmatic incompressible model with added dilatational terms. For effective calibration of the closure model coefficients, we extend fixed-point analysis to compressible SMC models. The pressure–strain correlation closure coefficients are established by requiring consistency between model fixed-point behaviour and compressible homogeneous shear DNS data at the self-similar asymptotic state. The closure coefficients are functions of gradient Mach number. The coefficients asymptote to very small values at high gradient Mach number indicating that pressure effects diminish at very high speeds. At low gradient Mach number, the coefficients tend to incompressible values. The pressure–dilatation model is obtained by simply taking the trace of the pressure–strain correlation closure expression. The dissipation equation is modified to account for the conversion of kinetic energy to internal energy by pressure–dilatation.

The model is validated against the high-speed mixing-layer data of Goebel & Dutton (1991), hypersonic-boundary-layer experiment of Owen & Horstman (1972), and supersonic-boundary-layer direct numerical simulation data of Duan *et al.* (2011). The main findings of the validation study are that as the relative Mach number of the mixing layer increases, the new model can adequately capture: (i) increasing Reynolds stress anisotropy; (ii) decrease in Reynolds shear stress; and (iii) consequent reduction in compressible mixing-layer growth rates. The boundary-layer results show adequate agreement with data, even without the use of sophisticated near-wall corrections.

One of the important simplifications invoked in this work is the use of the turbulence integral length scale in the definition of gradient Mach number, instead of the more precise acoustic length scale. A possible future direction is a new evolution equation for acoustic length scale. Indeed, this could be critically important for accurate compressible shear flow computations.

Acknowledgements

This work was supported by the National Aeronautics and Space Administration under contract number NASA-NRA NNX08AB44A with Dr D. Yoder as Program Monitor. Computational resources were provided by the Texas A&M Supercomputing Facility http://sc.tamu.edu/. C.A.G. gratefully acknowledges the support from CONACyT, Consejo Nacional de Ciencia y Tecnología. Both authors thank Dr S. Wallin of FOI, Swedish Defence Research Agency, for generous support in the use of the EDGE solver.

Appendix A

Three types of functions are used to find the least-squares curve fits of the calibrated pressure–strain correlation model coefficients shown in figure 5:

$$f_1 = a_1 \exp\left(a_2 M_g^*\right) + a_3 \exp\left(a_4 M_g^*\right), \tag{A 1}$$

Model	Coefficient	Type	R^2	a_1	a_2	a_3	a_4
GG-I	C_1/C_{1_0}	f_1	0.9981	0.2786	−4.7758	0.7213	−0.0334
	C_3/C_{3_0}	f_1	0.9785	0.9712	−1.4877	—	—
	C_4/C_{4_0}	f_1	0.9917	1.0232	−2.3907	—	—
	C_5/C_{5_0}	f_1	0.9951	0.9978	−2.2155	—	—
	C_P	f_2	0.9334	0.0342	0.2378	0.0981	—
GG-II	C_1/C_{1_0}	f_1	0.9981	0.2786	−4.7758	0.7213	−0.0334
	C_3/C_{3_0}	f_1	0.9575	0.9557	−1.5664	—	—
	C_4/C_{4_0}	f_1	0.9960	1.0111	−2.5253	—	—
	C_5/C_{5_0}	f_1	0.9904	0.9883	−2.3393	—	—
	C_P	f_3	0.9426	0.0105	1.8×10^{-6}	−0.3233	0.0452

TABLE 7. Least-squares coefficient curve fits.

$$f_2 = a_1 \exp\left[-\left(\frac{M_g^* - a_2}{a_3}\right)^2\right], \tag{A 2}$$

and

$$f_3 = \frac{a_1 M_g^* + a_2}{M_g^{*2} + a_3 M_g^* + a_4}, \tag{A 3}$$

where

$$M_g^* = \frac{M_g}{M_{g_{max}}}, \quad M_{g_{max}} = 3.05. \tag{A 4}$$

The fit coefficients a_1–a_4 as well as the coefficient of determination R^2 for each fit are provided in table 7. The coefficient of determination is computed using

$$R^2 \equiv 1 - \frac{SSE}{SST}, \quad SSE = \sum_{i=1}^{n} (y_i - \widehat{y}_i)^2, \quad SST = \sum_{i=1}^{n} (y_i - \overline{y})^2, \quad \overline{y} = \frac{1}{n}\sum_{i=1}^{n} y_i, \tag{A 5}$$

where y_i and $\widehat{y}_i$ refer to the original and fitted data points respectively. *SSE* is the residual sum of squares and *SST* is the total sum of squares.

Appendix B

The compressible pressure–strain correlation models GG-I and GG-II are implemented into the ANSYS® FLUENT Release 13.0 software package. Closure model modifications are incorporated into the solver via user-defined functions, UDFs. ANSYS® FLUENT (ANSYS 2010) solves evolution equations for mean mass (2.3), momentum (2.4), energy equation

$$\left.\begin{aligned} \frac{\partial}{\partial t}(\overline{\rho}E) + \frac{\partial}{\partial x_i}\left[\tilde{u}_i\left(\overline{\rho}E + \overline{p}\right)\right] &= \frac{\partial}{\partial x_j}\left[\left(\kappa + \frac{c_p \mu_t}{Pr_t}\right)\frac{\partial \tilde{T}}{\partial x_j} + \tilde{u}_i\left(\tau_{ij}\right)_{eff}\right], \\ E &= \tilde{h} - \frac{\overline{p}}{\overline{\rho}} + \frac{\tilde{u}_i \tilde{u}_i}{2}, \end{aligned}\right\} \tag{B 1}$$

$$\left(\tau_{ij}\right)_{eff} = \mu_{eff}\left(\frac{\partial \tilde{u}_i}{\partial x_j} + \frac{\partial \tilde{u}_j}{\partial x_i}\right) - \frac{2}{3}\mu_{eff}\frac{\partial \tilde{u}_k}{\partial x_k}\delta_{ij}, \tag{B 2}$$

$$\mu_t = \frac{\overline{\rho} C_\mu k^2}{\varepsilon}, \quad \mu_{eff} = \mu + \mu_t, \tag{B 3}$$

Reynolds stresses (2.14), and dissipation rate (3.11), shown as used for GG-II. For GG-I there is no C_P term in (3.11). The GG-I and GG-II calculations use their respective pressure–strain correlation coefficients that have been calibrated with DNS shown in figure 5. The least-squares curve fits for the coefficient calibrations can be found in appendix A. The production and transport tensors are defined in (2.15) and (2.20) respectively. The pressure–strain correlation is given by the sum of (3.6) and (3.7). In the calculations, air is used as the working fluid, and the molecular viscosity is computed using Sutherland's Law (Sutherland 1893)

$$\mu = \mu_0 \left(\frac{\tilde{T}}{T_0} \right)^{3/2} \left(\frac{T_0 + S_0}{\tilde{T} + S_0} \right). \tag{B 4}$$

Additional closure constants applicable to all models

$$\mu_0 = 1.716e-5 \text{ (kg (m s)}^{-1}\text{)}, \quad T_0 = 273.11 \text{ (K)}, \quad S_0 = 110.56 \text{ (K)}, \tag{B 5}$$

$$C_\mu = 0.09, \quad \sigma_k = 0.82, \quad \sigma_\varepsilon = 1.0, \quad Pr_t = 0.85. \tag{B 6}$$

For comparison, computations are also performed with the LRR (Launder *et al.* 1975) and SSG-S (Speziale *et al.* 1991; Sarkar 1992) models. The coefficients of these models are given in table 2. The SSG-S model uses the SSG (Speziale *et al.* 1991) pressure–strain correlation as well as the two main Sarkar compressibility corrections (Sarkar *et al.* 1991*a*; Sarkar 1992): pressure–dilatation shown in (4.30), and compressible dissipation given by

$$\varepsilon_c = \alpha_1 \varepsilon M_t^2. \tag{B 7}$$

In the present notation, the SSG-S pressure–strain correlation model is written as

$$\begin{aligned} \Pi_{ij} = &- \left(C_1 \overline{\rho}\varepsilon + C_1^* \overline{\rho} P\right) b_{ij} + C_2 \overline{\rho}\varepsilon \left(b_{ik}b_{kj} - \frac{1}{3} b_{mn}b_{mn}\delta_{ij} \right) + \left[C_3 - C_3^* \left(b_{ij}b_{ij} \right)^{1/2} \right] \overline{\rho} k S_{ij} \\ &+ C_4 \overline{\rho} k \left(b_{ik}S_{jk} + b_{jk}S_{ik} - \frac{2}{3} b_{mn}S_{mn}\delta_{ij} \right) + C_5 \overline{\rho} k \left(b_{ik}W_{jk} + b_{jk}W_{ik} \right) \\ &+ \left(2\alpha_2 \overline{\rho} k M_t \frac{\partial \tilde{u}_m}{\partial x_n} b_{mn} + \alpha_3 \overline{\rho}\varepsilon M_t^2 \right) \frac{2}{3}\delta_{ij}. \end{aligned} \tag{B 8}$$

The LRR model has the same form as equation (B 8), with model coefficients given in table 2. It must be noted that the LRR model involves no compressibility correction and its results are given only for comparison purposes.

REFERENCES

ADUMITROAIE, V., RISTORCELLI, J. R. & TAULBEE, D. B. 1999 Progress in Favré–Reynolds stress closures for compressible flows. *Phys. Fluids* **11** (9), 2696–2719.

ANSYS, 2010 *ANSYS® FLUENT Theory Guide*, ANSYS®, Inc, Southpointe 275 Technology Drive Canonsburg, PA 15317, Release 13.0.

AUPOIX, B. 2004 Modelling of compressibility effects in mixing layers. *J. Turbul.* **5**, N7.

BERTSCH, R. 2010 Rapidly sheared compressible turbulence: characterization of different pressure regimes and effect of thermodynamic fluctuations. Master's thesis, Texas A&M University.

BERTSCH, R. L., SUMAN, S. & GIRIMAJI, S. S. 2012 Rapid distortion analysis of high Mach number homogeneous shear flows: characterization of flow-thermodynamics interaction regimes. *Phys. Fluids* **24** (12), 125106.

BOWERSOX, R. D. W. 2009 Extension of equilibrium turbulent heat flux models to high-speed shear flows. *J. Fluid Mech.* **633**, 61–70.

CAMBON, C., COLEMAN, G. N. & MANSOUR, N. N. 1993 Rapid distortion analysis and direct simulation of compressible homogeneous turbulence at finite mach number. *J. Fluid Mech.* **257**, 641–665.

CHAOUAT, B. & SCHIESTEL, R. 2005 A new partially integrated transport model for subgrid-scale stresses and dissipation rate for turbulent developing flows. *Phys. Fluids* **17** (6), 065106.

CHINZEI, N., MASUYA, G., KOMURO, T., MURAKAMI, A. & KUDOU, K. 1986 Spreading of two-stream supersonic turbulent mixing layers. *Phys. Fluids* **29** (5), 1345–1347.

CLEMENS, N. T. & MUNGAL, M. G. 1995 Large-scale structure and entrainment in the supersonic mixing layer. *J. Fluid Mech.* **284**, 171–216.

CROW, S. C. 1968 Viscoelastic properties of fine-grained incompressible turbulence. *J. Fluid Mech.* **33**, 1–20.

DUAN, L., BEEKMAN, I. & MARTÍN, M. P. 2011 Direct numerical simulation of hypersonic turbulent boundary layers. Part 3. Effect of Mach number. *J. Fluid Mech.* **672**, 245–267.

DURBIN, P. A. & SPEZIALE, C. G. 1994 Realizability of second-moment closure via stochastic analysis. *J. Fluid Mech.* **280**, 395–407.

DURBIN, P. A. & ZEMAN, O. 1992 Rapid distortion theory for homogeneous compressed turbulence with application to modelling. *J. Fluid Mech.* **242**, 349–370.

ELIASSON, P. 2005 EDGE, a Navier–Stokes solver for unstructured grids. *Tech. Rep.* FOI-R-0298-SE. FOI.

ELIASSON, P. & PENG, S.-H. 2008 Drag prediction for the DLR-F6 wing-body configuration using the EDGE solver. *J. Aircraft* **45** (3), 837–847.

FREUND, J. B., LELE, S. K. & MOIN, P. 2000 Compressibility effects in a turbulent annular mixing layer. Part 1. Turbulence and growth rate. *J. Fluid Mech.* **421**, 229–267.

FUJIWARA, H., MATSUO, Y. & CHUICHI, A. 2000 A turbulence model for the pressure–strain correlation term accounting for compressibility effects. *Intl J. Heat Fluid Flow* **21** (3), 354–358.

GATSKI, T. B. & JONGEN, T. 2000 Nonlinear eddy viscosity and algebraic stress models for solving complex turbulent flows. *Prog. Aeronaut. Sci.* **36**, 655–682.

GATSKI, T. B. & SPEZIALE, C. G. 1993 On explicit algebraic stress models for complex turbulent flows. *J. Fluid Mech.* **254**, 59–78.

GERMANO, M. 1992 Turbulence: the filtering approach. *J. Fluid Mech.* **238**, 325–336.

GIRIMAJI, S. S. 1996 Fully explicit and self-consistent algebraic Reynolds stress model. *Theor. Comput. Fluid Dyn.* **8**, 387–402.

GIRIMAJI, S. S. 1997 A Galilean invariant explicit algebraic Reynolds stress model for turbulent curved flows. *Phys. Fluids* **9** (4), 1067–1077.

GIRIMAJI, S. S. 2000 Pressure-strain correlation modelling of complex turbulent flows. *J. Fluid Mech.* **422**, 91–123.

GIRIMAJI, S. S. 2004 A new perspective on realizability of turbulence models. *J. Fluid Mech.* **512**, 191–210.

GIRIMAJI, S. S. 2006 Partially-averaged Navier–Stokes model for turbulence: a Reynolds-averaged Navier–Stokes to direct numerical simulation bridging method. *Trans. ASME: J. Appl. Mech.* **73** (3), 413–421.

GIRIMAJI, S. S., JEONG, E. & SRINIVASAN, R. 2006 Partially-averaged Navier–Stokes method for turbulence: fixed point analysis and comparison with unsteady partially averaged Navier–Stokes. *Trans. ASME: J. Appl. Mech.* **73** (3), 422–429.

GOEBEL, S. G. & DUTTON, J. C. 1991 Experimental study of compressible turbulent mixing layers. *AIAA J.* **29** (4), 538–546.

HALL, J. L., DIMOTAKIS, P. E. & ROSEMANN, H. 1993 Experiments in nonreacting compressible shear layers. *AIAA J.* **31** (12), 2247–2254.

HELLSTEN, A. 2005 New advanced k–ω turbulence model for high-lift aerodynamics. *AIAA J.* **43** (9), 1857–1869.

HUANG, S. & FU, S. 2008 Modelling of pressure–strain correlation in compressible turbulent flow. *Acta Mechanica Sin.* **24** (1), 37–43.

JOHANSSON, A. V. & HALLBÄCK, M. 1994 Modelling of rapid pressure–strain in Reynolds-stress closures. *J. Fluid Mech.* **269**, 143–168.

JONES, W. P. & MUSONGE, P. 1988 Closure of the Reynolds stress and scalar flux equations. *Phys. Fluids* **31** (12), 3589–3604.

KHLIFI, H., ABDALLAH, J., AÏCHA, H. & TAÏEB, L. 2011 A priori evaluation of the Pantano and Sarkar model in compressible homogeneous shear flows. *C. R. Mec.* **339**, 27–34.

KIM, J. & PARK, S. O. 2010 New compressible turbulence model for free and wall-bounded shear layers. *J. Turbul.* **11** (10), 1–20.

KLINE, S. J., CANTWELL, B. J. & LILLEY, G. M. 1982*Proc. 1980-81 AFOSR-HTTM-Stanford Conf. on Complex Turbulent Flows, Vol. 1, Stanford University*.

LAUNDER, B. E., REECE, G. J. & RODI, W. 1975 Progress in the development of a Reynolds-stress turbulence closure. *J. Fluid Mech.* **68**, 537–566.

LAVIN, T. A., GIRIMAJI, S. S., SUMAN, S. & YU, H. 2012 Flow-thermodynamics interactions in rapidly-sheared compressible turbulence. *Theor. Comput. Fluid Dyn.* **26** (6), 501–522.

LEE, K. & GIRIMAJI, S. S. 2013 Flow-thermodynamics interactions in decaying anisotropic compressible turbulence with imposed temperature fluctuations. *Theor. Comput. Fluid Dyn.* **27** (1–2), 115–131.

LEE, K., GIRIMAJI, S. S. & KERIMO, J. 2008 Validity of Taylor's dissipation-viscosity independence postulate in variable-viscosity turbulent fluid mixtures. *Phys. Rev. Lett.* **101** (7), 074501.

LIEN, F. S. & LESCHZINER, M. A. 1994 Assessment of turbulent-transport models including nonlinear RNG eddy-viscosity formulation and second-moment closure for flow over a backward-facing step. *Comput. Fluids* **23** (8), 983–1004.

LIVESCU, D., JABERI, F. A. & MADNIA, C. K. 2002 The effects of heat release on the energy exchange in reacting turbulent shear flow. *J. Fluid Mech.* **450**, 35–66.

LIVESCU, D. & MADNIA, C. K. 2004 Small scale structure of homogeneous turbulent shear flow. *Phys. Fluids* **16** (8), 2864–2876.

LIVESCU, D. & RISTORCELLI, J. R. 2007 Buoyancy-driven variable-density turbulence. *J. Fluid Mech.* **591**, 43–71.

LIVESCU, D. & RISTORCELLI, J. R. 2008 Variable-density mixing in bouyancy-driven turbulence. *J. Fluid Mech.* **605**, 145–180.

LUMLEY, J. L. 1978 Computational modeling of turbulent flows. *Adv. Appl. Mech.* **18**, 123–176.

MARZOUGUI, H., KHLIFI, H. & LILI, T. 2005 Extension of the Launder, Reece and Rodi model on compressible homogeneous shear flow. *Eur. Phys. J.* B **45**, 147–154.

MENTER, F. R. 1994 Two-equation eddy-viscosity turbulence models for engineering applications. *AIAA J.* **32** (8), 1598–1605.

MISHRA, A. A. & GIRIMAJI, S. S. 2010 Pressure-strain correlation modeling: towards achieving consistency with rapid distortion theory. *Flow Turbul. Combust.* **85**, 593–619.

OWEN, F. K. & HORSTMAN, C. C. 1972 On the structure of hypersonic turbulent boundary layers. *J. Fluid Mech.* **53**, 611–636.

PANTANO, C. & SARKAR, S. 2002 A study of compressibility effects in the high-speed turbulent shear layer using direct simulation. *J. Fluid Mech.* **451**, 329–371.

PAPAMOSCHOU, D. & ROSHKO, A. 1988 The compressible turbulent shear layer: an experimental study. *J. Fluid Mech.* **197**, 453–477.

PARK, C. H. & PARK, S. O. 2005 A compressible turbulence model for the pressure–strain correlation. *J. Turbul.* **6** (2), 1–25.

PENNISI, S. & TROVATO, M. 1987 On the irreducibility of Professor G. F. Smith's representations for isotropic functions. *Intl J. Engng Sci.* **25**, 1059–1065.

POPE, S. B. 1975 A more general effective-viscosity hypothesis. *J. Fluid Mech.* **72** (2), 331–340.

POPE, S. B. 1994 Lagrangian PDF methods for turbulent flows. *Annu. Rev. Fluid Mech.* **26**, 23–63.

POPE, S. B. 2000 *Turbulent Flows*, 1st edn. Cambridge University Press.

REYNOLDS, W. C. 1976 Computation of turbulent flows. *Annu. Rev. Fluid Mech.* **8**, 183–208.

RISTORCELLI, J. R. 1993 A representation for the turbulent mass flux contribution to Reynolds-stress and two-equation closure for compressible turbulence. *ICASE Rep.* 93-88. NASA Langley Research Center, Hampton, VA.

RISTORCELLI, J. R., LUMLEY, J. L. & ABID, R. 1995 A rapid-pressure covariance representation consistent with the Taylor–Proudman theorem materially frame indifferent in the two-dimensional limit. *J. Fluid Mech.* **292**, 111–152.

RODI, W. 1976 A new algebraic relation for calculating the Reynolds stresses. *Z. Angew. Math. Mech.* **56**, T219–T221.

ROTTA, J. C. 1951 Statistiche theorie nichthomogener turbulenz. *Z. Phys.* **129**, 547–572.

SAMIMY, M. & ELLIOT, G. S. 1990 Effects of compressibility on the characteristics of free shear layers. *AIAA J.* **28** (3), 439–445.

SARKAR, S. 1992 The pressure-dilatation correlation in compressible flows. *Phys. Fluids* **4** (12), 2674–2682.

SARKAR, S. 1995 The stabilizing effect of compressibility in turbulent shear flow. *J. Fluid Mech.* **282**, 163–186.

SARKAR, S., ERLEBACHER, G. & HUSSAINI, M. Y. 1991*a* The analysis and modelling of dilatational terms in compressible turbulence. *J. Fluid Mech.* **227**, 473–493.

SARKAR, S., ERLEBACHER, G. & HUSSAINI, M. Y. 1991*b* Direct simulation of compressible turbulence in a shear flow. *Theor. Comput. Fluid Dyn.* **2**, 291–305.

SCHLICHTING, H. & GERSTEN, K. 2000 *Boundary Layer Theory*, 8th edn. Springer.

SIMONE, A., COLEMAN, G. N. & CAMBON, C. 1997 The effect of compressibility on turbulent shear flow: a rapid-distortion-theory and direct-numerical-simulation study. *J. Fluid Mech.* **330**, 307–338.

SJÖGREN, T. & JOHANSSON, A. V. 2000 Development and calibration of algebraic nonlinear models for terms in the Reynolds stress transport equations. *Phys. Fluids* **12** (6), 1554–1572.

SMITH, G. F. 1971 On isotropic funcions of symmetric tensors, skew-symmetric tensors and vectors. *Intl J. Engng Sci.* **9**, 899–916.

SMITS, A. J. & DUSSAUGE, J. 2006 *Turbulent Shear Layers in Supersonic Flow*, 2nd edn. Springer Science+Business Media.

SPEZIALE, C. G. 1991 Analytical methods for the development of Reynolds-stress closures in turbulence. *Annu. Rev. Fluid Mech.* **23**, 107–157.

SPEZIALE, C. G., GATSKI, T. B. & SARKAR, S. 1992 On testing models for the pressure–strain correlation of turbulence using direct simulations. *Phys. Fluids* **4** (12), 2887–2899.

SPEZIALE, C. G., SARKAR, S. & GATSKI, T. B. 1991 Modelling the pressure–strain correlation of turbulence: an invariant dynamical systems approach. *J. Fluid Mech.* **227**, 245–272.

SUMAN, S. & GIRIMAJI, S. S. 2010 On the invariance of compressible Navier–Stokes and energy equations subject to density-weighted filtering. *Flow Turbul. Combust.* **85** (3), 383–396.

SUTHERLAND, W. 1893 The viscosity of gases and molecular force. *Phil. Mag. Ser.* 5 **36** (223), 507–531.

TAVOULARIS, S. & CORRSIN, S. 1981 Experiments in nearly homogeneous shear flow with a uniform mean temperature gradient. Part 1. *J. Fluid Mech.* **104**, 311–347.

THACKER, W. D., SARKAR, S. & GATSKI, T. B. 2007 Analyzing the influence of compressibility on the rapid pressure–strain rate correlation in turbulent shear flows. *Theor. Comput. Fluid Dyn.* **21** (3), 171–199.

VREMAN, A. W., SANDHAM, N. D. & LUO, K. H. 1996 Compressible mixing layer growth rate and turbulence characteristics. *J. Fluid Mech.* **320**, 235–258.

WALLIN, S. & JOHANSSON, A. V. 2000 An explicit algebraic Reynolds stress model for incompressible and compressible turbulent flows. *J. Fluid Mech.* **403**, 89–132.

WALZ, A. 1969 *Boundary Layers of Flow and Temperature*, 1st edn. MIT.

WHITE, F. M. 1991 *Viscous Fluid Flow*, 2nd edn. McGraw-Hill.

WILCOX, D. C. 1988 Reassesment of the scale-determining equation for advanced turbulence models. *AIAA J.* **26** (11), 1299–1310.

WILCOX, D. C. 1993 *Turbulence Modelling for CFD*, 1st edn. DCW Industries.